Chapter 1 Introduction

1.1 Introduction to nanotechnology

Nanostructures that are defined as having at least to 1 and 100 nm one dimension have received much interest as a result of their peculiar and fascinating properties, and applications superior to their bulk counterparts.[1-3] The ability to generate such nanostructure is essential to much of modern science and technology.

Recently, one dimension nanostructures such as wires, belts, rods, and tubes have also become the focus of intensive research owing to their unique applications in meso-scopic physics and fabrication of nanoscale devices.[5] Many unique and fascinating properties have already been proposed or demonstrated for this class of materials, such as superior mechanical toughness,[6] higher luminescence efficiency, [7] enhancement of thermoelectric figure of merit, [8] and a lowered lasing threshold. [9] Previously, nanowires with different compositions have been explored using various methods, including vapor phase transport process,[10-13] chemical vapor deposition, [13-14] arc-discharge,[15] laser ablation,[14,16] solution[7,17] and template based methods. [18-19] Meanwhile, most of these works has been focused on semiconductor systems such as Si, [5,14] Ge, [10] GaN, [11] and GaAs, [5,13] until recently that 1D oxide nanostructures have become the very promising nanoscale building blocks because of their interesting properties, diverse functionalities, surface cleanness and chemical/thermal stability.[22,23,9,12,20,21]

1.2 Motivation

Zinc oxide is a wide band gap (3.37eV) semiconductor, for which ultraviolet lasing action has been reported in disordered particles and thin films. [24-26] In this regard, ZnO is a good candidate for room temperature UV lasing as its exciton binding energy is approximately 60meV, significantly larger than that of ZnSe(22meV) and GaN(25meV). Recently, many groups grew ZnO nanowires on sapphire or silicon by simple vapor transport and condensation process via vapor-liquid-soild mechanism or by MOVPE via vapor-solid mechanism.[10,62]

In this study we choice another substrate, porous silicon, to grow ZnO nanowires. Porous silicon is one of Si-based materials and conforms to today's Si-industry. It is an anisotropy crystalline, and we can easily control the surface morphology of porous phase via different current density. We expect that Au dots as catalyst will be different on porous and pure silicon substrates while forming ZnO nanowires. And the surface morphology of an porous silicon substrate plays a major role in controlling the growth of low dimensional structures.[27] In general, the anisotropy of the surface can influence the growth via at least two major mechanisms: firstly, it can eliminate an anisotropic strain of nanowires grown on a lattice mismatched interface, and secondly, it can confine the adatom diffusion to lower dimensions.[28-29] Thus, it is expected that the surface feature of an anisotropic crystalline substrate can control the growth behavior of 1D nanowires.

1.3 Organization of the thesis

The thesis consists of five chapters, including the present introduction. Next chapter introduces the growth mechanism of vapor liquid solid method (VLS), as well as the basic theory of some characterization tools for semiconductors such as x-ray

diffraction (XRD) spectrum, photoluminescence (PL) spectrum. In Chapter 3, we describe the experimental details, including sample preparation, the equipment setups and parametric characterization. By means of the XRD and PL, the crystalline changes under different growth conditions have been investigated and discussed. The morphology and detailed structure of ZnO nanowires are also investigated by SEM and TEM. In the final chapter, we give a conclusion to our investigations on the ZnO nanowires and some proposal topics for further study.

Chapter 2. Theoretical background

2.1 Vapor-Liquid-Solid Methods

Among all vapor based methods, the VLS method seems to be the most successful in generating nanowires with single crystalline qualities and in relatively large quantities. This process was originally developed by Wagner and his co-workers to produce micrometer-sized whisker in 1960s.[33] Recently, this technique is re-examined by Lieber, Yang, and many research groups to produce nanowires and nanorods from a rich variety of inorganic materials.[10,16,34-37] A typical VLS process starts with the dissolution of gaseous reactants into nanosized liquid droplet of a catalyst metal, and then followed by nucleation and growth of single crystalline nanorods and nanowires. The 1D growth is mainly induced and dictated by the liquid droplets, the size of which remain essentially unchanged during the entire process of nanowire growth. In the sense, each liquid droplet serves as a soft template to limit strictly the lateral growth of an individual nanowire. As a major requirement, there should exist a good solvent capable of forming liquid alloy with the growing material, ideally they should be able to form eutectic compounds. All major steps involved in a VLS process schematically illustrated in Fig.2-1. Based on the Zn-Au binary phase diagram (Fig.2-2), Zn and Au form liquid alloys when the temperature is raised above the eutectic point. Once the liquid droplet is supersaturated with Zn, nanowire growth will begin to occur at solid liquid interface. The vapor pressure of Zn in the CVD system has to be kept sufficiently low that second ordinary nucleation events will be completely suppressed. Both physical methods (thermal evaporation, laser ablation) and chemical methods(chemical vapor transport and deposition) have been employed to generate the vapor species required for the growth of nanowires, and no significant difference was found in the quality of nanowires produced by these methods.

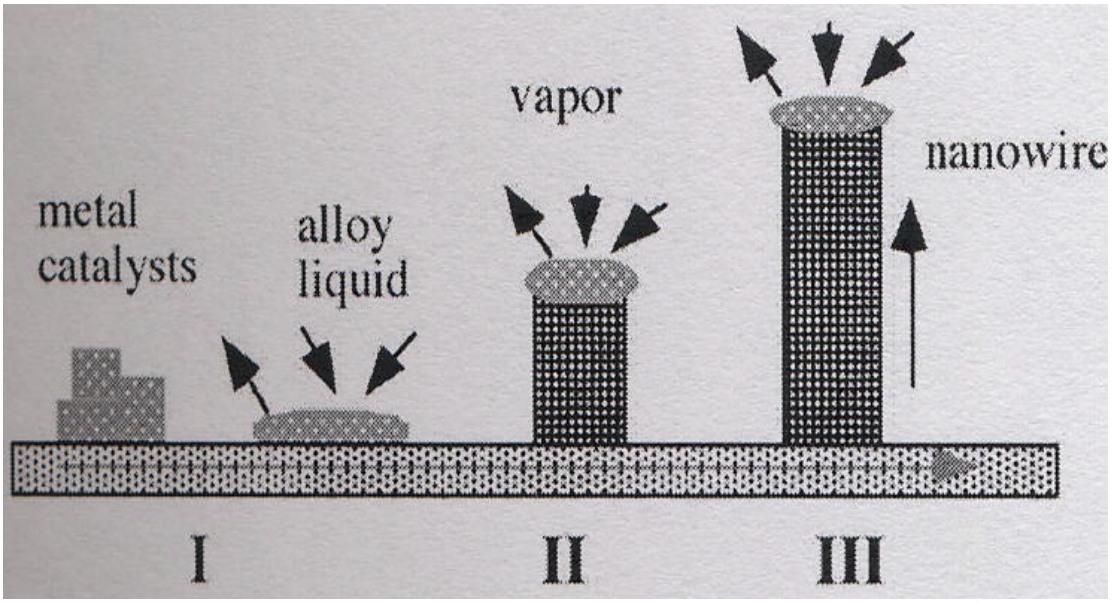

Fig.2-1 VLS method

I : Au-Zn alloying

II: ZnO nucleation

III: ZnO nanowire growth

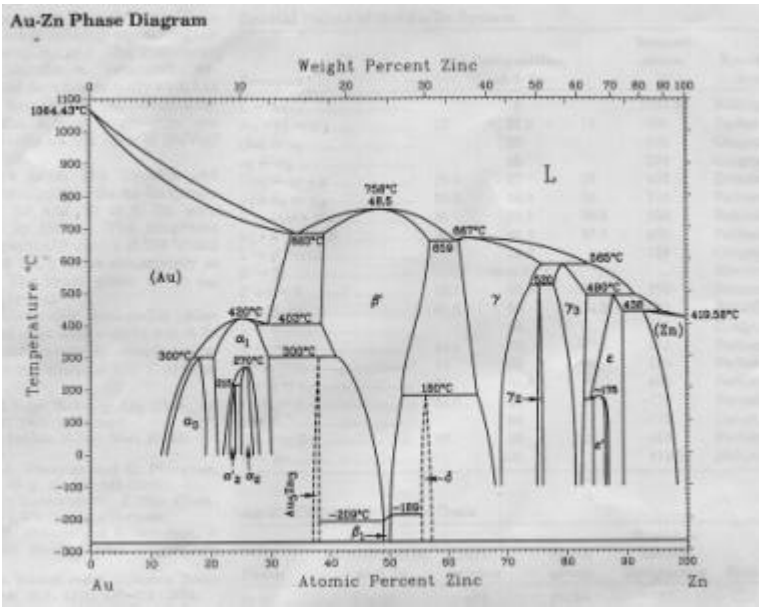

Fig.2-2 Au-Zn phase diagram

2.2 The formation of porous silicon

Porous silicon (PS) is formed by an electrochemical etching of Si in an HF solution. Following anelectrochemical reaction occurring at the Si surface a partial dissolution of Si settles in. The exact dissolution chemistries of Si are still in question, and different mechanisms have been proposed. However, it is generally accepted that holes are required for both electropolishing and pores formation. During pore formation two hydrogen atoms evolve for every dissolved Si atom.[38,39] The hydrogen evolution diminishes while F^- ion approaching the electropolishing regime and disappears during electropolishing. Current efficiencies are about two electrons per dissolved Si atom during pore formation, and about four electrons in the electropolishing regime.[38,40,41] The global anodic semi-reactions can be written during pore formation as

$$Si + 6HF \rightarrow H_2SiF_6 + H_2 + 2H^+ + 2e^-$$

and during electropolishing as

$$Si + 6HF \rightarrow H_2SiF_6 + 4H^+ + 4e^-$$

The final and stable product for Si in HF is in any case H_2SiF_6 or some of its ionized forms. This means that during pore formation only two of the four available Si electrons participate in an interfacial charge transfer, while the remaining two undergo corrosive hydrogen liberation. In contrast, during electropolishing, all four Si electrons are electrochemically active. Lehmann and Gosele [42] have proposed a dissolution mechanism that is so far the most accepted (Fig.2-3). It is based on a surface bound oxidization scheme, with hole capture, and subsequent electron injection, which leads to the divalent Si oxidization state.

According to Fig.2-3, the Si hydride bonds passivate the Si surface unless a hole is available. This hypothesis is also supported by the experimental observation that hydrogen gas continues to evolve from the porous layer after the release of the applied potential for a considerable time. In addition, various spectroscopic techniques have confirmed the presence of Si-H surface bonds during PS formation.[43,44] While it is generally accepted that pore initiation occurs at surface defects or irregularities, different models have been proposed to

explain pore formation in PS.[40,42,45] Some basic requirements have to be fulfilled for electrochemical pore formation to occur:[46]

1. Holes must be supplied by bulk Si, and be available at the surface.
2. While the pore walls have to be passivated, the pore tips have to be active in the dissolution reaction. Consequently, a surface which is depleted of holes is passivated to electrochemical attach, which means that (i) the electrochemical etching is self-limiting and (ii) hole depletion occurs only when every hole that reaches the surface reacts immediately. The chemical reaction is not limited by mass transfer in the electrolyte.
3. The current density should be lower than the electropolishing critical value.

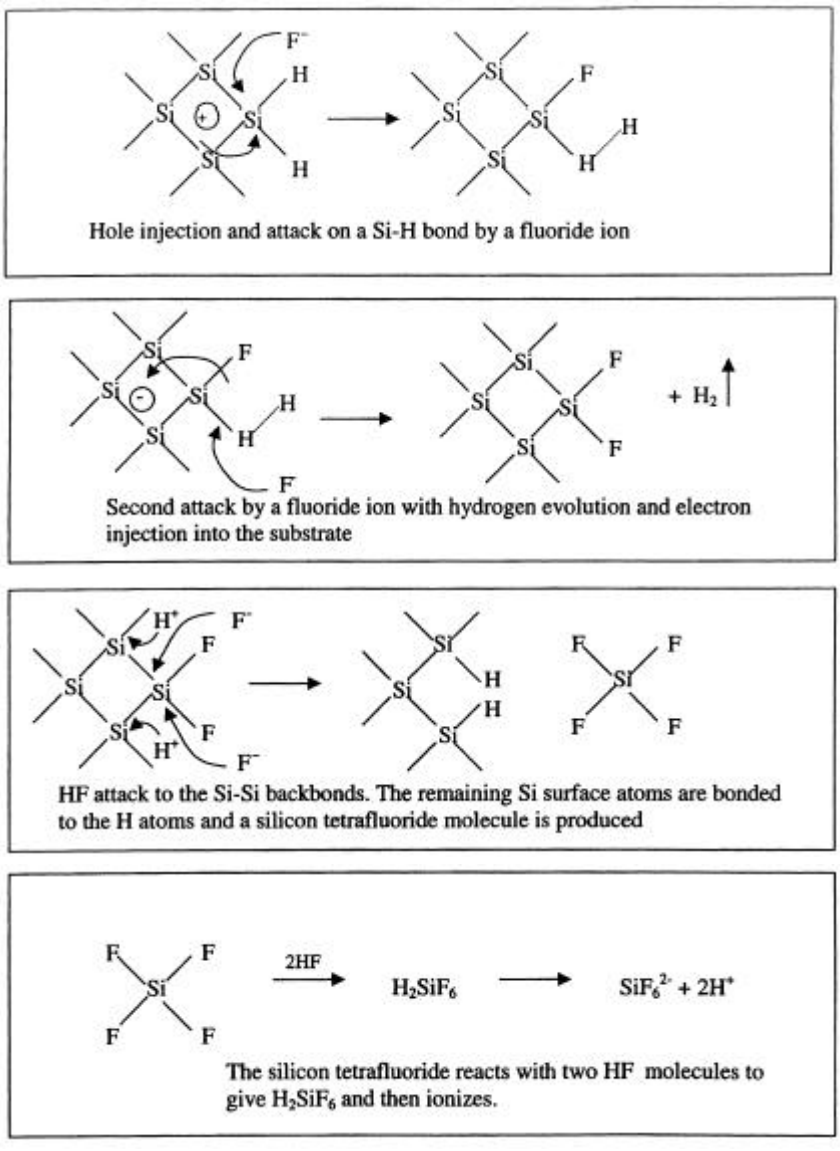

Fig.2-3 the process of PS

2.3 X-ray diffraction

Considering now the path difference between successive planes when the incident beam remains fixed at the Bragg angle θ as in Fig. 2-4, but with the diffracted ray leaving at an angle $\theta+\Delta\theta$, corresponding to the intensity I in the spectrum line an angular distance $\Delta\theta$ away from the peak. The path difference between waves from successive planes is now[47)]

$$BC + CE = d \cdot \sin q + d \cdot \sin(q + \Delta q)$$
$$= d \cdot \sin q + d \sin q \cos \Delta q + d \cos q \sin \Delta q \qquad (2\text{-}1)$$

with BC and CE is the path difference between the successive incident beams, and d is the interplanar distance. If $\Delta\theta$ is not too large, we can write $\cos\Delta\theta \cong 1$ and $\sin\Delta\theta \cong \Delta\theta$, in which case

$$BC + CE = 2d \sin q + d \cos q \cdot \Delta q$$
$$= n l + d \cos q \cdot \Delta q, \qquad (2\text{-}2)$$

where λ is the wavelength of the incident X-ray. Therefore the phase δ per interplanar distance is

$$d = \frac{2p}{l} n l + \frac{2p}{l} d \cos q \cdot \Delta q$$
$$= 2pn + \frac{2p}{l} d \cos q \cdot \Delta q. \qquad (2\text{-}3)$$

Since a phase difference of $2\pi n$ produces the same effect as a zero phase, we can write the effective phase difference as

$$d = \frac{2p}{l} d \cos q \cdot \Delta J. \qquad (2\text{-}3)$$

We obtained the result that the distribution of intensity I in a spectrum line a distance R from the grating is effectively

$$I = \left(\frac{f}{R}\right)^2 \frac{\sin^2 \frac{1}{2} Nd}{\sin^2 \frac{1}{2} d} \qquad (2\text{-}4)$$

and the maximum intensity is

$$I_{\max} = (\frac{f}{R})^2 N^2, \qquad (2\text{-}5)$$

where Φ is the amplitude at unit distance from the grating, N the total number of grating apertures, and δ the phase change per aperture. Diving (2-4) by (2-5), we obtain

$$\frac{I}{I_{\max}} = \frac{1}{N^2}\frac{\sin^2 \frac{1}{2}Nd}{\sin^2 \frac{1}{2}d}. \qquad (2\text{-}6)$$

Since (1/2)Nδ will change much faster than (1/2) δ, the function will reach its first minimum before (1/2) δ is very large. If we replace sin(1/2δ by (1/2) δ, we obtain

$$\frac{I}{I_{\max}} = (\frac{\sin \frac{1}{2}Nd}{\frac{1}{2}Nd})^2. \qquad (2\text{-}7)$$

The ratio I/I_{max} will fall to 1/2 when

$$\frac{\sin \frac{1}{2}Nd}{\frac{1}{2}Nd} = \frac{1}{\sqrt{2}}. \qquad (2\text{-}8)$$

The solution to the equation yields the required phase change corresponding to the half maximum. It may be obtained

$$\frac{1}{2}N\frac{2p}{l}d\cos q\Delta q = 1.39 \qquad (2\text{-}9)$$

or, since D= Nd

$$2\Delta q = \frac{0.89l}{D\cos q}. \qquad (2\text{-}10)$$

Let β_s be the full width at half maximum from Δθ to −Δθ then

$$b_s = \frac{0.89l}{D\cos q} \quad (\text{radians}), \qquad (2\text{-}11)$$

where λ is the wavelength of the x-ray source, and D is the size of the particles.

Considering hexagonal unit cell which is characterized by lattice parameters a_0 and c_0. The plane spacing equation for the hexagonal structure is

$$\frac{1}{d^2}=\frac{4}{3}\left(\frac{h^2+hk+k^2}{a^2}\right)+\frac{l^2}{c^2}. \qquad (2\text{-}12)$$

Combining Bragg ' s law (λ =2 d sin θ) with (2-12) yields :

$$\frac{1}{d^2}=\frac{4}{3}\left(\frac{h^2+hk+k^2}{a^2}\right)+\frac{l^2}{c^2}=\frac{4\sin^2 q}{l^2}. \qquad (2\text{-}13)$$

Rearranging (2-13) gives

$$\sin^2 q=\frac{l^2}{4}\{\frac{4}{3}\left(\frac{h^2+hk+k^2}{a^2}\right)+\frac{l^2}{c^2}\}, \qquad (2\text{-}14)$$

thus the lattice parameters can be estimated from (2-14).

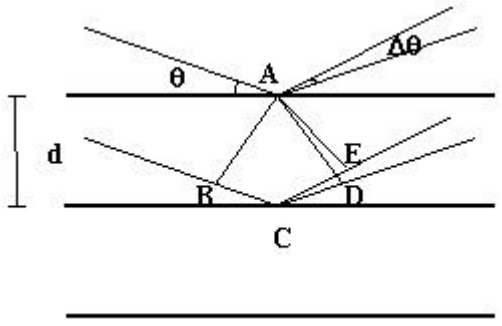

Fig.2-4 the crystalline planes of the materials

2.4 Photoluminescence Characterization

Photoluminescence (PL) is very useful and powerful optical methods in the semiconductor industry, with its sensitive ability to find the emission mechanism and band structure of semiconductors. From photoluminescence the defect or impurity can also be found in the compound semiconductors, which affect materials quality and device performance. A given impurity produces a set of characteristic spectral features. The fingerprint identifies the impurity type, and often several different impurities can be seen in a single PL spectrum. In addition, the full width of half magnitude of each PL peak is an

indication of sample ' s quality, although such analysis has not yet become highly quantitative.[48)]

Photoluminescence is the optical radiation emitted by a physical system (in excess the thermal equilibrium blackbody radiation) resulting from excitation to a nonequilibrium state by irradiation with light. Three processes can be distinguished: (i) creation of electron-hole pairs by absorption of the excited light, (ii) radiative recombination of electron-hole pairs, and (iii) escape of the recombination radiation from the sample. Since the excited light is absorbed in creating electron-pair pairs, the greatest excitation of the sample is near the surface; the resulting carrier distribution is both inhomogeneous and nonequilibrium. In attempting to regain homogeneity and equilibrium, the excess carriers will diffuse away from the surface while being depleted by both radiative and nonradiative recombination processes. Most of the excitation of the crystal is thereby restricted to a region within a diffusion length (or absorption length) of the illuminated surface. Consequently, the vast majority of photoluminescence experiments are arranged to examine the light emitted from the irradiated side of the samples. This is often called front surface photoluminescence.

Since emission requires that the system be in a nonequilibrium condition, and some means of excitation is acting on the semiconductor to produce hole-electron pairs. We consider the fundamental transitions, those occurring at or near the band edges.

1. Free excitons

A free hole and a free electron as a pair of opposite charges experience a coulomb attraction. Hence the electron can orbit about the hole as a hydrogen-like atom.

If the material is sufficiently pure, the electrons and holes pair into excitons which then recombine, emitting a narrow spectral line. In a direct-gap semiconductor, where momentum is conserved in a simple radiative transition,

the energy of the emitted photon is simply

$$h\nu = E_g - E_x$$

where E_g and E_x are the band gap and the exciton binding energy

2. Bound excitons:

Similar to the way that free carriers can be bound to (point-) defects, it is found that excitons can also be bound to defects. A free hole can combine with a neutral donor to form a positively charged excitonic ion. In this case, the electron bound to the donor still travels in a wide orbit about the donor. The associated hole which moves in the electrostatic field of the " fixed " dipole, determined by the instantaneous position of the electron, then also travels about this donor; for this reason, this complex is called a " bound exciton ". An electron associated with a neutral acceptor is also a bound exciton. The binding energy of an exciton to a neutral donor (acceptor) is usually much smaller than the binding energy of an electron (hole) to the donor (acceptor).

3. Donor-Acceptor Pairs

Donors and acceptors can form pairs and act as stationary molecules imbedded in the host crystal. The coulomb interaction between a donor and an acceptor results in a lowering of their binding energies. In the donor-acceptor pair case it is convenient to consider only the separation between the donor and the acceptor level:

$$E_{pair} = E_g - (E_D + E_A) + \frac{q^2}{e\ r},$$

where r is the donor-acceptor pair separation, E_D and E_A are the respective ionization energies of the donor and the acceptor as isolated impurities.

4. Shallow transitions

The shallow transitions to neutralize ionized donors or acceptors are shown

in Fig. 2-5. It is conceivable that these transitions could be radiate in the far infrared.

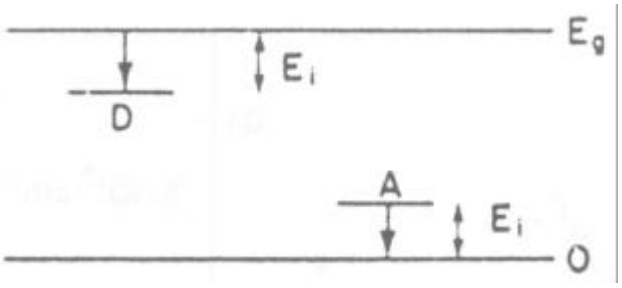

Fig. 2-5 Shallow transitions

5. Deep transitions

By deep transition we shall mean either the transition of an electron from the conduction band to an acceptor state or a transition from a donor to the valence band in Fig. 2-6. Such transition emit a photon $h\nu=E_g - E_i$ for direct transitions and $h\nu=E_g - E_i - E_p$ if the transition is indirect and involves a phonon of energy E_p. Hence the deep transitions can be distinguished as (1) conduction-band-to-acceptor transition which produces an emission peak at $h\nu=E_g - E_A$, and (2) donor-to-valence-band transition which produces and emission peak at the higher photon energy $h\nu=E_g - E_D$.

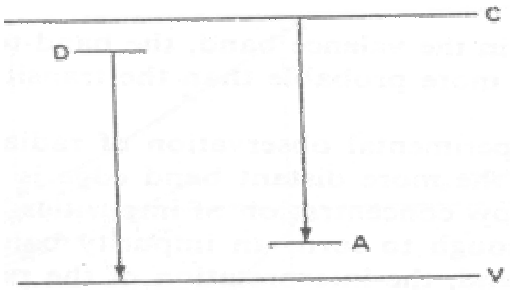

Fig. 2-6 Radiative transition between a band and an impurity state.

6. Transitions to deep levels

Some impurities have large ionization energies; therefore, they form deep levels in the energy gap. Raditive transitions between these states and the band edge emit at $h\nu=E_g - E_i$.[49)]

2.5 Scanning electron microscopy

The principle of the SEM, used for examining a solid specimen in the emissive mode, is closely comparable to that of a closed circuit TV system shown in Fig.2-7. In the TV camera, light from the object forms an image on a special screen, and the signal from the screen depends on the image intensity at the point being scanned. The signal is used to modulate the brightness of a cathode ray tube (CRT) display, and the original image is faithfully reproduced if (a) the camera and display raster are geometrically similar and exactly in time, and (b) the time for signal collection and processing is short compared with the time for the scan move from one picture point to the next.

In the SEM the object itself is scanned with the electron beam and the electrons emitted from the surface are collected and amplified to form the video signal. The emission varies from point to point on the specimen surface and so an image is obtained. Many different specimen properties cause variations in electron emission and so, although information might be obtained about all these properties, the images need interpreting with care. The resolving power of the instrument can not be smaller than the diameter of the electron probe scanning across the specimen surface, and a small probe is obtained by the demagnification of the image of an electron source by means of electron lenses. The lenses are probe forming rather than image forming, and the magnification of the SEM image is determined by the ratio of the sizes of raster scanned on the specimen surface and on the display screen.

Fro example, if the image on the CRT screen is 100mm across, magnifications of 100X and 10000X are obtained by scanning areas on the specimen surface 1mm and 10 μ m across, respectively. One consequence is that high magnifications are easy to obtain with the SEM, while very low magnifications are difficult. This is because large angle deflections are required which imply wide bore scan coils and other problem parts, and it is more difficult to maintain scan linearity, spot focus and efficient electron collection at the extremes of the scan.

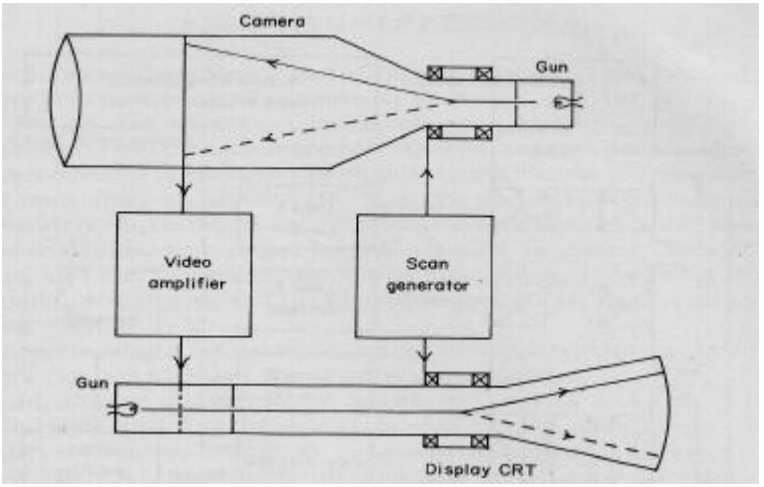

Fig.2-7 (a) Closed circuit TV

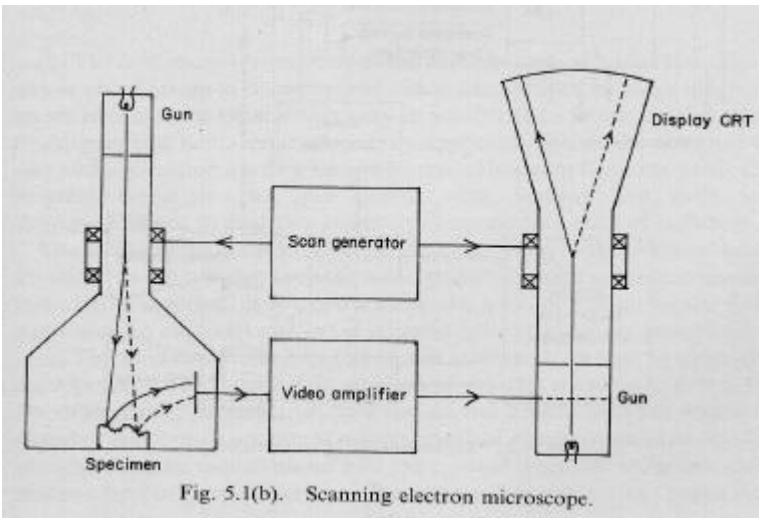

Fig.2-7 (b) Scanning electron microscope

Chapter 3 Experimental details

3.1 Sample preparations

3.1.1 porous silicon substrate preparation

The porous silicon substrate was formed by the electrochemical anodization method on a <100>p+ type silicon substrate. Fig.3-1 shows our experimental tank used for electrochemical anodization method in this study. All the substrate having area of 1 cm^2 were placed in the tank vertically. The distance between platinum electrode and silicon substrate is 5 cm. The anodic etching was carried out in the HF-ethanol solution (HF: ethanol=1:1) with different current density of 10mA/cm^2 , 20mA/cm^2 , 40mA/cm^2 , 80mA/cm^2 .

3.1.2 Au thin film preparation

All the substrates having area of 1 cm^2 were cleaned before coating Au thin film by the following steps:

(1) Rinsed in D. I. water in 5min.

(2) Rinsed in H_2SO_4:H_2O_2=1:1 in 15min.

(3) Repeat step(1)

(4) Rinsed in HF:H_2O=1:100 in 15min.

(5) Repeat step(1)

(6) Rinsed in H_2O:H_2O_2:NH_4OH=1:1:5 in 15min

(7) Repeat step(1)

(8) Rinsed in H_2O:H_2O_2:HCl=1:1:6 in 15min

(9) Repeat step(1)

(10) Rinsed in HF:H_2O=1:100 in 15min.

(11) Dried with the gas of N_2

After initial RCA clean, we used RF-sputter to coat Au thin film. Coating time was 5 sec and the thickness of Au thin film was about 100 A.

3.1.3 ZnO nanowire growth

After coating Au thin film, we mixed ZnO powder and graphite (weight ratio=1:1) powder and put them on the alumina boat. The alumina boat carrying the Au-coated substrates were placed into a quartz tube. The substrates were placed 25-30cm from the center of the boat. This quartz tube was placed inside a furnace, with the center of the alumina boat positioned at the center of the furnace and the substrates placed downstream of an argon flow (Fig.3-2). The quartz tube was kept 1-30 torr. The temperature of the furnace was ramped to 950^0C at a rate of $20\text{-}30^0 C min^{-1}$ and then kept at that fixed temperature for 2-4hr under a constant flow of argon (150sccm). After the furnace was cooled to the room temperature, dark gray material was obtained on the surface of the substrates.

3.2 X-ray diffraction

After growing the ZnO nanowires, the crystal structures of the as-grown ZnO nanowires were inspected by X-ray diffractometer a JPN MAC Science MXP18 with a CuK α line (λ=1.5405Å). The maximum voltage of the system is 30kV with a maximum current 20mA. The scanning step is 0.02^0 and scanning rate is 4^0 /min.

3.3 Scanning Electron Microscope system

The morphology of ZnO nanowires were observed by the Field Emission Gun Scanning Electron Microscopy (FEG-SEM) The accelerated voltage is 0.5-30kV and the magnification is 10-500k times. Besides, the Energy Dispersive X-ray Analyzer (EDX) is also another function of SEM and the composition of the ZnO nanowires can be identified by EDX.

3.4 Transmission electron microscope system

The detailed structure of ZnO nanowires can be found by transmission electron microscope. The TEM images were taken by a Hitachi electron microscope operated at 125 kV. The prepared nanowires were firstly suspended in alcohol by supersonic jolt and then the suspension was moved to the copper grid for observation.

3.5 Photoluminescence detection system

A He-Cd laser (Kimmon IK5552R-F) operating at the 325 nm UV line is commonly utilized as a pumping source for PL. As shown in Fig. 3-3, the PL detection system includes reflection mirror, focusing and collecting lens, the sample holder and the cooling system.

In this system, we utilized two single-grating monochromators (TRIAX 320), one equipped with a CCD detector (CCD-3000), and the other equipped with a photo-multiplier tube (PMT-HVPS), which are matched with a photon counter for detection. The normal operated voltage of PMT is 0.8 KV. Moreover, we used a standard fluorescent lamps to calibrate our spectral response of spectrometer and detector. PL signals are exposed about 0.1 sec at a step of 0.1 nm,

and the data are transmitted through a PGIB card and recorded by a computer. The monochromator (TRAIX 320) is a 32 cm one with three selective resolutions of lines 600, 1200 and 1800 grooves/mm separately. When the entrance and exit slits are both opened to about 50 μm, the resolution is about 0.1 nm in this system. Low-temperature PL measurements were able to carry out by using an additional closed cycle cryogenic system.

Flowchart

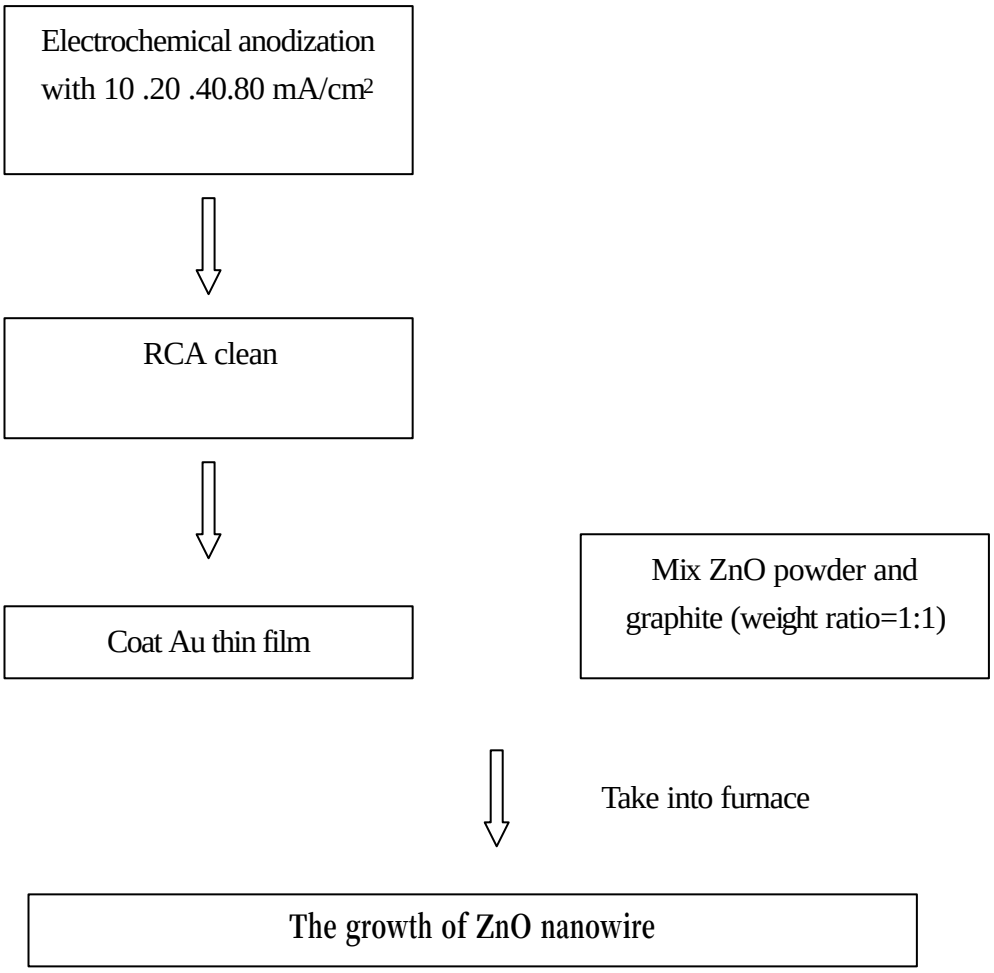

The condition of growth: pressure=10 torr

Argon flow=150sccm

Chapter 4. Results and discussion

4.1 Growth parameters of the ZnO nanowire

4.1.1 Pressures dependence on optical properties of ZnO nanowire

Fig.4-1~4-2 show PL spectral patterns of ZnO nanowires grown on silicon substrates pored with J=10mA/cm^2 by VLS method under the tube pressures of (a) 1 (b) 5 (c) 10 (d) 30 Torr at a fixed flux rate of argon gas 150 sccm. From the PL pattern, we can observe the three main photon emission categories: the near band edge emission (NBE) with peak position of 3.263 eV, the low energy tail extending from the near band edge emission, and the deep level emission with peak position of 2.48 eV at room temperature. We used the least square method to decouple the NBE and low energy tail extending from the NBE shown in the insert of Fig.4-1. Under the growth pressure of 10 Torr the FWHM of the NBE feature is corresponding to 98meV. From Fig4-2 we find the FWHM of NBE becomes larger when the growth pressure is higher or lower than 10 Torr. The concentration of Zn vapor generated with the thermal reduction of ZnO powder by carbon depends on the tube pressure. When the concentration of Zn vapor is too high or low, the growth of ZnO nanowires is not proper. Because too much Zn vapor will make the Au-Zn alloys quickly to be saturated, the ZnO nucleation will be completed too fast to be a good single crystalline nanowire. And the appropriate growth rate is necessary for the ZnO nanowires growth. As the pressure is too low the ZnO nucleation will be completed too slowly to be a good single crystalline nanowire. So the concentration of Zn vapor must be appropriate for growing ZnO nanowires. Besides, we also observe ZnO nanowires on the porous silicon substrates with different current density show the

different FWHM of NBE. The reason is that the lattice mismatch between ZnO and PS substrate is bigger as the current density is larger. As increasing current density, the surface roughness of PS is more obvious. So the surface roughness perhaps is another reason.

4.1.2 Flow dependence on optical properties of ZnO nanowire

As indicated above, although optimal growth pressure can make ZnO nanowires have the better performance, the highly textured ZnO nanowires was still hardly obtained by using appropriate argon gas flow. So we used a sequence of different argon gas flow to grow better quality ZnO nanowires. Fig.4-3 shows the PL spectra obtained from ZnO nanowires grown under the tube pressure of 10 Torr at argon flow of 125, 150, 200, 250 sccm. The NBE intensity and the full width at half maximum both increase with the increasing argon gas flow as shown in Fig.4-4. When argon flow is higher than 150sccm, the FWHM increases and the crystalline structure of nanowire becomes poor. Because when argon gas flow is higher than 150sccm, too much Zn vapor carried by argon gas is making the nucleation fast. The crystalline structure with fast nucleation in ZnO nanowires does not give a good optical property. The FWHM of NBE is broader than that of lower argon gas flow. We also found the ZnO nanowires did not grow on the PS substrate as the argon gas flow is lower than 100sccm. We speculate that Zn vapor is too low to make Zn in the Au-Zn alloy to be saturated, and there for Zn can not nucleate on the Au-Zn alloy surface to form ZnO.

4.1.3 Growth temperature dependence on optical properties of ZnO nanowire

The substrate temperature is one of the important factors during the growth

of ZnO nanowires. When the substrate temperature is higher than 750^0C, Au still forms Au-Zn alloy with Zn. But it doses not form ZnO nanowires. Fig.4-5 shows only Au-Zn droplets-like alloy on the substrate (indicated by arrow) and there is no ZnO nanowires . Because the solubility of Zn in Au-Zn droplets is higher at high temperature, it is not supersaturated and Zn vapor does not nucleate at the solid-liquid interface. But when the substrate temperature is decreased to lower temperature (~650^0C), the solubility of Zn in the Au-Zn alloys decrease and then supersaturated Zn alloys forms. It makes Zn start to oxidize and forms ZnO nanowires. When the temperature is much lower than 650^0C, Zn separates fast from the Au-Zn alloys due to the low solubility of Zn at low temperature. That produces the poor crystalline structure of ZnO nanowires and not only nanowires but also other blocks or films exist.

4.1.4 Thickness of Au thin film dependence on optical properties of ZnO nanowire

According to the above optimal growth condition: tube pressure 10 Torr, argon flow rate 150sccm, substrate temperature 700^0C, different thickness of Au thin film was changed to grow ZnO nanowires. The SEM images for a series of Au thickness in growing nanowires were shown in Fig.4-6~4-8. From SEM images we can observe the thicker thickness of Au film, the smaller diameter ZnO nanowires were obtained by CVD. The experiment results are analogous to other group's results.[31)] It is strange that the ZnO belts and nanowires were grown together on the thicker thickness of Au thin film shown in Fig.4-8. We speculate that the thicker Au thin film forms bigger Au clusters or islands closely with each others at high temperature, that makes each Au-Zn alloys to connect together. Consequently, the piece of Zn reacts with oxides to form the ZnO belts.

4.2 Result of the X-ray diffraction measurement

The X-ray diagrams measured from CVD grown nanowires are shown in Fig.4-9(30^0~40^0). It shows XRD pattern of ZnO nanowires grown by CVD under a fixed 10 Torr pressure and at a fixed 150sccm argon flow. Chemical vapor deposited nanowires exhibit virtually identical diffraction patterns of a wurtzite phase and in concurrence with results obtained previously. Three main diffraction peaks (1)31.6^0[100], (2)34.4^0[002], (3)36.1^0[101] were found evident as comparing with JCPDs data. By comparing with ZnO nanowires grown on sapphire, only [002] orientation has been measured, our nanowires seemed to have poor orientation preference due to the lattice mismatch between PS ans ZnO nanowires.

Besides, in order to understand whether the nanowires have orientation preference or not, we calculate the texture coefficient $T_{c(0\ 0\ 2)}$.[51] This factor can be calculated using the following formula:

$$T_{c(hkl)} = \frac{I_{(hkl)} / I_{0(hkl)}}{\frac{1}{N}\sum_N \left(\frac{I_{(hkl)}}{I_{0(hkl)}}\right)}$$

where $T_{c(h\,l\,k)}$ is the texture coefficient of (h k l) plane, I the measured intensity, I_0 the corresponding recorded ASTM intensity, and N the number of preferred growth directions. According to the XRD patterns from Fig.4-9(a)~(b) we can calculate the $T_{c(0\ 0\ 2)}$. The results are as listed in Table4-1(a)~(b). We can find the results are all larger than one. So the nanowires have a little orientation preference for [002]. And from the Table4-1(a) we find some texture coefficients are smaller. From Fig.4-35~4-38 we also find that the ZnO nanowires look like a group of groves. So we speculate that the reason caused lower texture coefficient is that the nanowires grew along the horizontal direction. So the XRD patterns look like the results of ZnO powder. Each diffraction patterns of ZnO can be measured. From Table4-1(b) we find

texture coefficient of ZnO nanowires grown on PS substrates is larger than on silicon substrate. We speculate that PS have lower Young's modulus to release stress between ZnO nanowires and substrate.[52,53] From below equations:

$$E_0 = E_{si}(1-P)^2$$

$$e_f = \frac{1}{1+\frac{E_f h_f}{E_0 d_0}} e_m$$

where E_{si} , E_f: Young's modulus of silicon and ZnO, P: porosity, e_m: total mismatch stress, h_f: length of ZnO , d_0: thickness of PS layer, e_f: efficient stress. We simplify the equation as

$$e_f \propto \frac{1}{1+\frac{1}{(1-P)^2}}$$

We find that the bigger porosity caused the lower stress between nanowires and substrate. So ZnO nanowires can grow along it's preference orientation [002]. But when silicon pored with higher current density, the surface roughness will be so violent that nanowires can not grow along it's preference orientation.

4.3 Photoluminescence spectra of ZnO nanowires

The photoluminescence of nanowires were measured using an He-Cd laser as the excitation source. Fig.4-10 shows the room temperature PL spectra of nanowires grown on the different porous silicon substrates: (a)10, (b)20, (c)40, (d)80 mA/cm^2. Strong emission at ~380nm is measured for all samples. The FWHM of NBE are (a)81, (b)81.8, (c)82.2, (d)83.5 meV. Comparing with our group's result,60 meV, we think them as proper samples. And we speculate the reason, making the FWHM bigger as current density increasing, the lattice mismatch between nanowires and PS substrate. In addition, we observe that the green emission intensity at ~510 nm

is very weak. While the UV emission corresponds to the near band edge emission, the green emission peak is commonly referred to as deep level or trap state emission. The green transition has been attributed to the singly ionized oxygen vacancy in ZnO and emission results from the radiative recombination of a photo-generated hole with an electron occupying the oxygen vacancy.[54] Fig.4-11 shows photoluminescence spectra of ZnO nanowires at 7 K. The sample was prepared at the optimal condition:10torr, 150sccm, 4hrs. From SEM images we think the structure proper. The insert in Fig.4-11 shows, in a logarithmic scale, the NBE at 7 K. The NBE including the emissions from the free exciton(EX) recombination located at 3.372eV with a FWHM of 9.082 meV and the another main peaks (3.362, 3.358eV), with the FWHM of 9.985,7.436 meV, which are attributable to a transition from an exciton bound to a neutral donor. The low energy extending tail of the band edge is attributable to emission from the longitudinal phonon replicas (LO) of free exciton (EX), as shown in the inset of Fig.4-11. The observation of the free exciton peak for ZnO nanowires at 7 K strongly suggests that the nanowires are of high optical quality.

In order to make sure what the origin is about each emission peak we use the model calculated by T. Schmidt, K. Lischka and W. Zulehner.[55] The luminescence intensity I of the NBE PL emission line is proportional to L^k, where L is the power of the exciting laser radiation. This k can be calculated using the following formula:

$$I \sim L^k$$

After calculation we can see the results from Table4-2 and Fig.4-12~4-14. Our results of calculation for each emission peak all lie between one and two. Therefore we can define them as exciton-like transitions.

Fig.4-15~4-16 show a series of photoluminescence measurements at temperature of 7~300 K and temperature-dependent PL peak intensities of ZnO nanowires. We observe that the intensity of the PL peak at 3.372 eV(EX) increases

with temperature increasing from 7 to 10 K but the intensities of the peaks at 3.362 and 3.358 eV decrease. This behavior presumably results from decomposition of bound excitons due to the increasing thermal energy, and hence supports the argument that the PL corresponds to a free exciton peak and the others to bound exciton peaks. Above 70 K, the intensities of the exciton recombination peaks also show a decrease with increasing temperature because of thermally induced dissociation of electron-hole pairs. However, the free exciton peak extends to room temperature, in contrast to those of the two bound ones disappearing around 150 K.

Then we perform numerical analyses of the energy position of the free exciton(EX) as function of temperature using a model which is a modification of Varshin equation for band gap temperature dependence:

$$E(T) = E(0) - \frac{aT^2}{b+T}. \qquad (1)$$

We obtain the band gap of ZnO from above equation (1) by fitting: 3.372 eV shown in Fig.4-17. Similar energy band gap (E_0=3.380 eV) had been produced from C. Boemare et al.[56)]

We also want to fit the temperature dependence of the free exciton emission intensities. In some conditions, the population governing a certain transition is given by:[57)]

$$\partial n/\partial t = G - n/t_R - n/t_{NR},$$

where n is the density of the minority carrier or exciton concerned, G is the generation rate, t_R and t_{NR} are radiative and nonradiative lifetimes, respectively. Nonradiative recombination rate is generally thermally activated (whether they correspond to level depopulation or to the activation of a nonradiative recombination center), i.e., $1/t_{NR} = 1/t_0 \exp(-E_a/kT)$. Under steady state, and since PL intensities are proportional to n/t_R, one obtains the Arrhenius expression:

$$I = I_0 /[\ 1+a \exp(-E_a/kT)] \qquad (2)$$

with a $=t_R /t_0$. E_a is the activation energy of the process. By the analysis of the Arrhenius plot of the integrated intensity of the free exciton, activation energy of about 55.711 meV is obtained in Fig. 4-18, the quantity is consistent with the free exciton binding energy 60 meV, which further supports our assignment. We also use the same method to calculate the activation energy of the bound excitons shown in Fig.4-19~4-20. We table the activation energy of bound excitons as Table4-3. The results correspond to the difference between the photon energy of free exciton and that of bound excitons. So we can make sure that the results are all right.

Besides, we calculate the exciton-phonon coupling constant, S.[58] The intensity distribution of the phonon replicas is determined by S. For the case of relatively strong coupling, the emission intensity of the n_{th} phonon replica I_n(?) and the principle emission line (Io) is related by

$$I_n = I_o \frac{S^n}{n!} \qquad \text{n=0, 1, 2…..}$$

From Fig.4-11, we obtain the coupling factor S=0.251 for free exciton. Comparing with the ZnO thin film grown on the sapphire by our lab, the coupling factor S=0.213. So we speculate that the exciton-phonon coupling effect in nanowires is more violent due to the spatial confinement.

When we change the excitation power, we find the peak energies of free and bound exciton decreases with increasing excitation power density, shown in Fig.4-21. It could be suggested that the redshift of the exciton peaks are caused by local heating effects. It could also support the exciton-exciton interaction. The interaction among excitons results in higher effective exciton temperatures above nominal crystal temperature of 7 K.[59,60] These excitons are said or be in a “hot”, nonthermalized state.

4.4 Results of SEM

4.4.1 SEM

The size of ZnO nanowires are about 30~100 nm in diameter and 2~3 μm in length as seen from field-emission scanning electron microscope(FE-SEM) shown in Fig.4-22~4-25. From SEM images we observe that the density of ZnO nanowires is lower for the higher porosity substrate. We speculate that the Au clusters are formed on the surface of silicon but not in the pores. So ZnO nanowires grew on the surface of silicon. This explains the fact that a higher porosity substrate causes a lower density nanowires. Comparing with results in growing ZnO nanowires on pure silicon under the same conditions, our SEM image, as shown in Fig.4-26, clearly indicates that nanowires are divided into two categories: ~20 nm in diameter and ~5 μm in length, ~50 nm in diameter and ~1 μm. The nanowires grown on PS show a better similarity in diameter and length. This can be explained by the different Au clusters formed on PS and silicon at high temperature. From Fig.4-27~4-28, we found that the size of Au clusters on PS is more uniform than those on silicon.

Besides, from the cross-section SEM shown in Fig.4-29~4-32 we found that the thickness of wetting layer is more on pure silicon than PS. We speculate that appropriate wetting layer is good to grow nanowires.

4.4.2 EDX

We used the EDX to check the growth mechanism of our ZnO nanowires. From Fig.4-39 we find that the tips of ZnO nanowires contain Au content, so we can define the growth method as the VLS one with Au as the catalyst element. Besides, we also make sure that the constituent components in nanowires are ZnO only as seem in Fig.4-40.

4.5 Results of TEM

The detailed structure of individual ZnO nanowires have been characterized using selected area electron diffraction(SED), high-resolution TEM(HR-TEM). These nanowires are monolithically single crystalline as evidenced by the SAED pattern shown in the insert of Fig.4-41. From Fig.4-41 we clearly find that the diameter of a nanowire is about ~50nm.

Chapter5. Conclusion and perspectives

5.1 Conclusion

The single crystal ZnO nanowires can be grown on the porous silicon substrate via a VLS method by chemical vapor deposition. A room temperature PL spectrum of the nanowires consists of a sharp UV emission band at ~380 nm and a very weak green emission band at 510 nm. From the RT-PL analysis, we found the optimum growth conditions for producing ZnO nanowires under P_{tube}=10 Torr, argon flow=150sccm and T=700^0C. The ZnO nanowires with a FWHM of 98meV at 3.263 eV were obtained.

According the XRD patterns and the texture coefficient we know that the nanowires possess certain of orientation preference for [002]. And ZnO nanowires grown on PS substrate have better texture coefficient than on silicon substrate. From low temperature PL spectrum we can observe the appearance of donor-bounded, free exciton and one appended with few LO-phonon replicas. The FWHM of free exciton emission is 9.082 meV. With increasing temperature, the intensities of bound excitons decay and finally only the free exciton appears. The band gap value obtained from Vaeshni formula fitting is 3.372 eV. The activation energy of free exciton also obtained by Arrhenius expression is 55.711 meV.

According to SEM images we can observe that nanowires are about 30~100 nm in diameter and 2~3 μm in length. We also find that the nanowires are more uniform on PS substrate than on silicon substrate. Besides, we speculate that ZnO nanowires are single crystalline from the SAED.

5.2 perspectives

In this research, our major objective is to grow the highly quality ZnO nanowires by CVD and analyze its optical properties. To achieve this goal, we need the triple harmonic of Nd-YAG laser (350nm, 10-ns pulse width) to offer higher excitation pumping source. It excites our samples and makes the nanowires produce stimulated emission. Besides, we require the near- field scanning optical microscope (NSOM) to study the localization and the divergence of the laser beam emitted from nanowires.

Reference:

1.a) Handbook of nanostructured materials and nano-technology(Ed: H.S. Nalwa), Acasmeic Press, New York 2000

b) Nanostructured materials: clusters, composites, and thin film(Ed: V.M. Shalaev, M. Moskovits), American chemical society, Washington ,DC 1997

c)Nanomaterials: synthesis, properties, and applications(Ed: A.S. Edelstein, R.C. Cammarata), Institute of physics, Philiadelphia, PA 1996

2.a) Aspecial issue on nanoscale materials, Acc. Chem. Res. 1999,32

b) P. Alivisatos, P.F. Barbara, A.W. Castleman, J. Chang, D.A. Dixon, M.L. Kline, G. L. McLendon, J.S. Miller, M.A. Ratner, P. J. Rossky, S.I. Stupp, M.I. Thompson, Adv. Mater. 1998, 10, 1297

c) Special issue on nanostructured materials, Chem. Mater. 1996, 8, 1569

d) G. A. Ozin, Adv. Mater. 1992, 4, 612

3.a)R. Dagani, C&EN News 2000, October, 27

b)A. Thiaville, J. Miltat, Science 1999, 284, 1939

4.a) Future trends in microelectronics: the nano millennium(Eds: S. Luryi, J. Xu, A. Zaslavsky), Wiley-Interscience, New Youk 2002

b) Special issue of Nature, 2000, 406, 1021

5.a) Z. L. Wang, Adv. Mater. 2000, 12, 1295

b) J. Hu, T. W. Odom, C. M. Lieber, Acc. Chem. Res. 1999, 32,435

c) A special issue in MRS Bull. 1999, 24, pp.20-49

6. E. W. Wang, P. E. Sheehan, C.M. Lieber, Science 1997, 277, 1971

7. J. D. Holmes, K. P. Johnston, R. C. Doty, B. A. Korgel, Science 2000, 287, 1471

8. L. D. Hicks, M. S. DresselhHaus, Phys. Rev. B 1996, 47, 16631

9. M. Huang, S. Mao, H. Feick, H. Yan, Y. Wu, H. Kind, E. Weber, R. Russo, P. Yang, Science 2001, 292, 1897

10. a) Y. Wu, P. Yang, Chem. Mater. 2000, 12, 605.
b) Y. Wu, P. Yang, J. Am. Chem. Soc. 2001, 123, 3165

11. C. C. Chen, C. C. Yeh, Adv. Mater. 2000, 12, 738

12. M. H. Huang, Y. Wu, H. Feick, E. Weber, P. Yang, Adv. Mater. 2001, 13, 113

13. M. Yazawa, M. Koguchi, A. Muto, M. Ozawa, K. Hiruma, Appl. Phys. Lett. 1992, 61, 2051

14. Y. Wu, R. Fan, P.Yang, Nano lett. 2002, 2, 83

15. Y. C. Choi, W. S. Kim, Y. S. Park, S. M. Lee, D. J. Bae, Y. H. Lee, G. S. Park, W. B. Choi, N.S. Lee, J. M. Kim, Adv. Mater. 2000, 12, 746

16.a) X. F. Duan, C. M. Lieber, Adv. Mater. 2000, 12, 746

b) A. M. Morales, C. M. Lieber, Science 1998, 279, 208

17. T. J. Trentler, K. M. Hickman, S. C. Goel, A. M. Viano, P. C. Gibbons, W. E. Buhro, Science 1995, 270, 1791
18.a) M. H. Huang, A. Choudrey, P. Yang, Chem Commun. 2000,12, 1603
b) J. Zhu, S. Fan, J. Mater. Res. 1999,14, 1175
19.Y. Li, G. W. Meng, L. D. Zhang, F. Philipp, Appl. Phys. Lett. 2000, 76, 2011
20. P. Yang, C. M. Lieber, Science 1996, 273, 1836
21. Z. W. Pan, Z. R. Dai, Z. L. Wang, Science 2001, 291, 1947
22. Y. Wu, H. Yan, P. Yang, Chem. Eur. J. 2002, 8, 1260
23. P. Yang, Y. Wu, R. Fan, Int. J. Nanosci. 2002. in press
24. H. Cao, J. Y. Xu, D. Z. Zhang, S. H. Chang, S. T. Ho, E. W. Seeling, X. Liu, R. P. H. Chang, Phys. Rev. Lett. 2000, 84, 5584
25. D. M. Bagnall, Y. F. Chen, Z. Zhu, T. Yao, S. Koyama, M. Y. Shen, T. Goto, Appl. Phys. Lett. 1997, 70, 2230
26. P. Yu, Z. K. Tang, G. K. L. Wong, M. Kawasaki, A. Ohtomo, H. Koinuma, Y. Segawa, J. Cryst. Growth 1992, 117, 753
27. F. J. Himpsel, A. Kirakosian, J. N. Crain, J. L. Lin, D. Y. Petrovykh, Solid State Commun. 2001, 117, 149
28. E. Bauer, Z. Kristallogr.110(1958) 395
29. J. Tersoff, R. M. Tromp, Phys. Rev. Lett. 1993, 70, 2782
30. Y. Xia, P. Yang, Y. Sun, Y. Wu, B. Mayers, B. Gates, Y. Yin, F. Kim, H. Yan, Adv. Mater. 2003, 15, 353
31. P. Yang, H. Yan, S. Mao, R. Russo, J. Johnson, R. Saykally, N. Morris, J. Pham, R. He, H. J. Choi, Adv. Mater. 2002,12, 323
32. J. S. Lee, M. Kang, S. Kim, M. S. Lee, Y. K. Lee, J. Crystal Growth 2003, 249, 201.
33. R. S. Wagner, W. C. Ellis, Appl. Phys. Lett. 1964, 4, 89
34. Elemental semiconductors: a) Y. J. Zhang, Q. Zhang, N. L. Wang, Y. J. Yan. H. H. Zhou, J. Zhu, J. Crystal Growth 2001, 226, 185. b) J. Weswater, D. P. Gosain, S. Tomiya, S. Usui, J. Vac. Sc. Techmol. 1997, B15, 554
35. a) C. C. Chen, C. C. Yeh, C. H. Chen, M. Y. Yu, H. L. Liu, J. J. Wu, K. H. Chen, J. Y. Peng, T. F. Chen, J. Am. Chem. Soc. 2001,123, 2791. b) J. Zhang, X. S. Peng, X. F. Wang, Y. W. Wang, L. D. Zhang, Chem. Phys. Lett. 2001,345, 372. c) M. Q. He, P. Z. Zhou, S. N. Mohammad, G. L. Harris, J. B. Halpern, R. Jacobs, W. L. Sarney, L. Salamanca-Riba, J. Crtst. Growth 2001, 231, 375. d) W. S. Shi, Y. F. Zheng, N. Wang, C. S. Lee, S. T. Lee, J. Vac. Sci. Tech. B 2001, 197,1115.
36. a)Y. W. Wang, L. D. Zhang, C. H. Liang, G. Z. Wang, X. S. Peng, Chem. Phys. Lett. 2002, 357, 314. b)Y. W. Wang, G. W. Meng, L. D. Zhang, C. H. Liang, Chem. Mater. 2002, 14, 1773

37.a) Y. J. Chen, J. B. Li, Y. S. Han, X. Z. Yang, J. H. Dai, J. Cryst. Growth 2002, 245, 163. b) X. C. Wu, W. H. Song, K. Y. Wang, T. Hu,B. Zhao, Y. P. Sun, J. J. Du, Chem. Phys. Lett. 2001, 336, 53
38. C. Pickering, M.I.J. Beale, D.J. Robbins, P.J. Pearson, R. Greef, J. Phys. C 1984,17, 6535.
39. M.J. Eddowes, J. Electroanal. Chem. 1990,280, 297.
40. M.I.J. Beale, J.D. Benjamin, M.J. Uren, N.G. Chew, A.G. Cullis, J. Crystal Growth 1985,73, 622.
41. V. Lehmann, H. Foll, J. Electrochem. Soc. 1990,37, 653.
42. V. Lehmann, U. Go»sele, Appl. Phys. Lett. 1991,58, 856.
43. A. Venkateswara, F. Ozanam, J.N. Chazalviel, J. Electrochem. Soc.1991, 138, 153.
44. L.M. Peter, D.J. Blackwood, S. Pons, Phys. Rev. Lett. 1989,62,308.
45. R.L. Smith, S.F. Chuang, S.D. Collins, J. Electron. Mater. 1988,138, 533.
46. U. Go»sele, V. Lehmann, in: L.T. Canham (Ed.), Properties of Porous Silicon, IEE INSPEC, The Institution of Electrical Engineers, London, 1997, p. 17.
47. A. Taylor: X-ray Metallography(John Wiley and Sons, New York, 1961) p.676
48. Optical characterization of semiconductors: infaraed, Raman, and Pholuminescence spectroscopy (Sidney Perlpwotz, USA,1993)p.61
49.Optical processes in semiconductors, Jacques I. Pankove, New York, 1971, p.107
50.Electron Microscopy and Microanalysis of Crystalline Materials(J. A. Belk)
51. J. Lu , Appl. Surface Sci. 2003,207, 295
52. Belmont, Bellet, Brechet, J. Appl. Phys. 1996, 79, 7589
53.P.L. Novikov,
54. K. Vanheusden, W. L. Warren, C. H. Seaqer, D. R. Tallant, J. A. Voigt, B. E. Gnage, J. Appl. Phys. 1996, 79, 7983
55. T. Schmidt, K. Lischka, W. Zulehner, Phys. Rev. B 1992, 45, 8989
56. C. Boemare, T. Monteiro, M. J. Soares, J. G. Guilerme, E. Alves, Physica B 2001,308-310,985
57. M. Leroux, N. Grandjean, B. Beaumont, G. Nataf, F. Semond, J. Msddied, P. Gibart, J. App. Phys. 1999, 86, 3271
58. C. Boemare, T. Monteiro, M.J. Soares, J.G. Guilherme, E. Alves, Physica B 2001,308-310, 985
59. J. Z. Wan, J. L. Brebner, R. Leonelli, G. Zhao, J. T. Graham, Phys. Rev. B 1993, 48, 5197
60. M. O. Godzaev, B. E. Sernelius, Phys. Rev. B 1987, 36, 9589
61. J. Z. Wan, J. L. Brebner, R. Leonelli, G. Zhao, J. T. Graham, Phys. Rev. B 1996, 53, 15413

62. W. I. Park, D. H. Kim, S.-W. Jung, and Gyu-Chul Yi, Applied Phys lett 2002,80, 4232

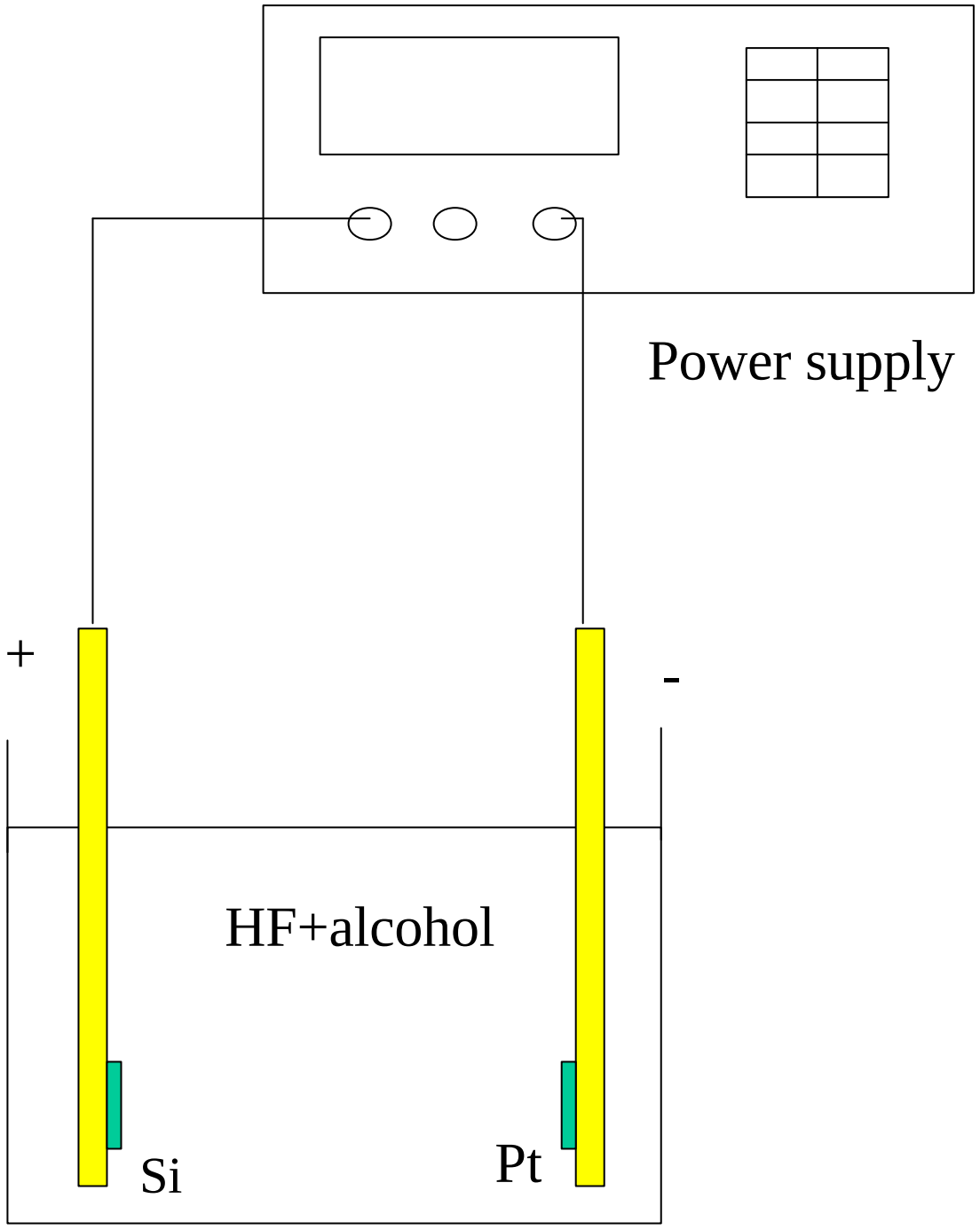

Fig.3-1 the anodic etching system

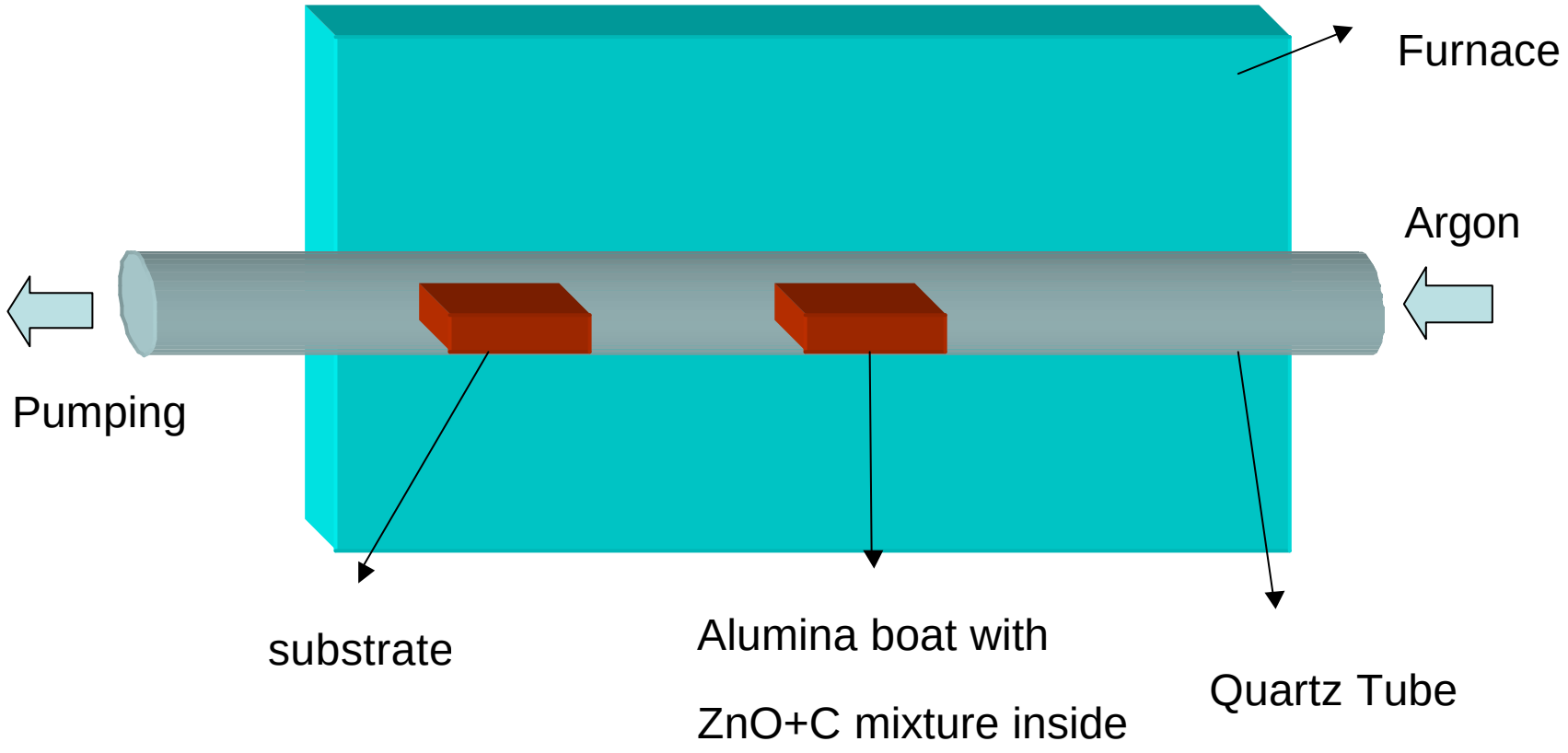

Fig.3-2 Chemical vapor transport and condensation system(CVTC)

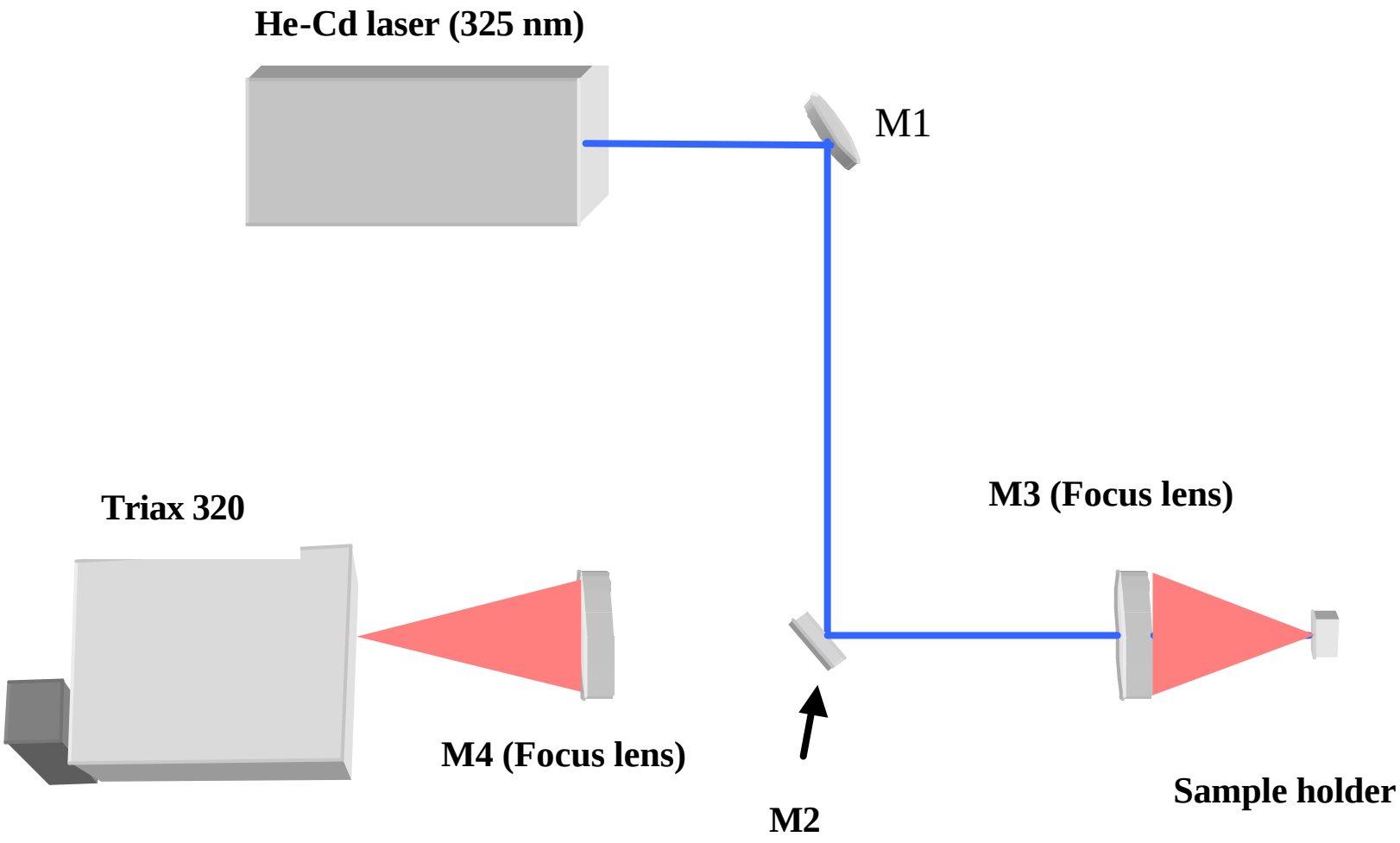

Fig.3-3 PL detection system

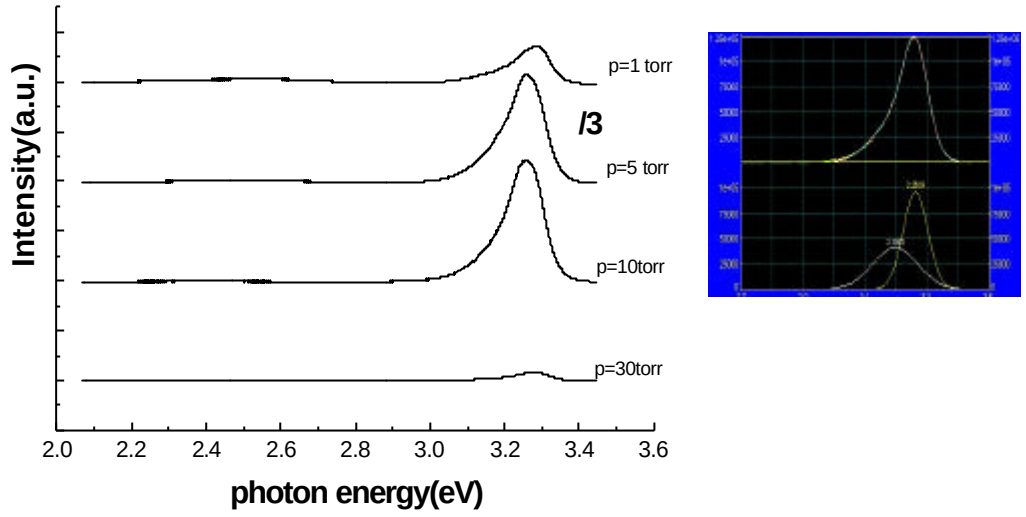

Fig.4-1: A series of substrate pressure dependent PL patterns under a growth condition of the fixed 150sccm argon flow at the same growth time 2hr.

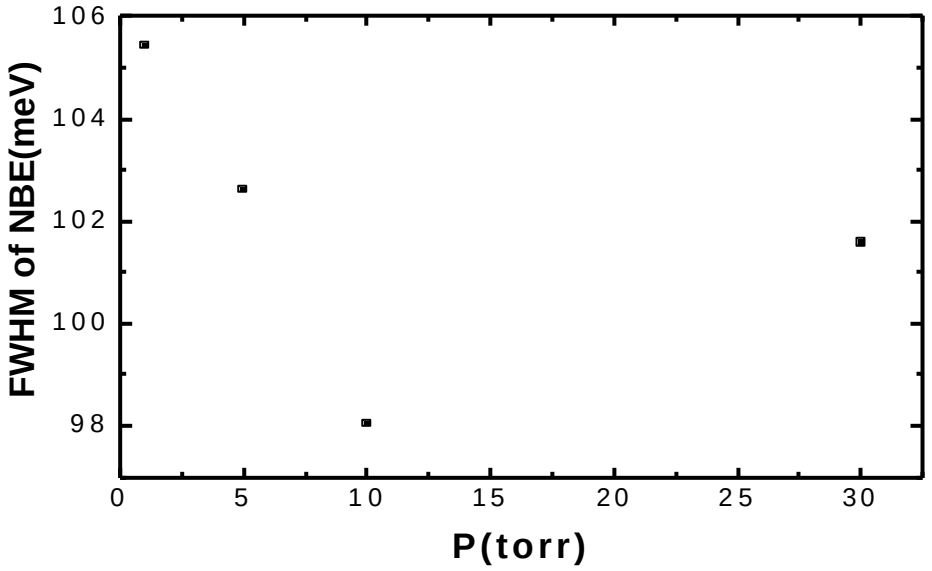

Fig.4-2: Growth pressure dependent ZnO PL peak FWHM.

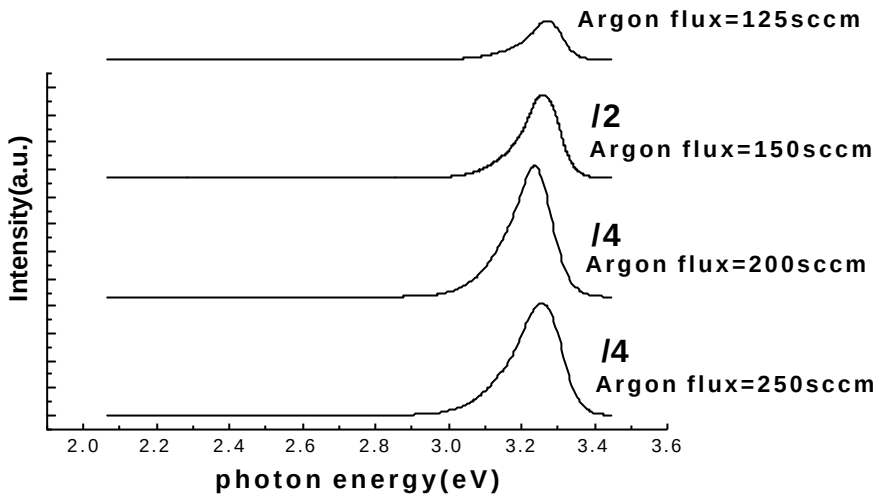

Fig.4-3: A series of substrate argon flow dependent PL patterns under a growth condition of the fixed 10 torr pressure at the same growth time 2hr.

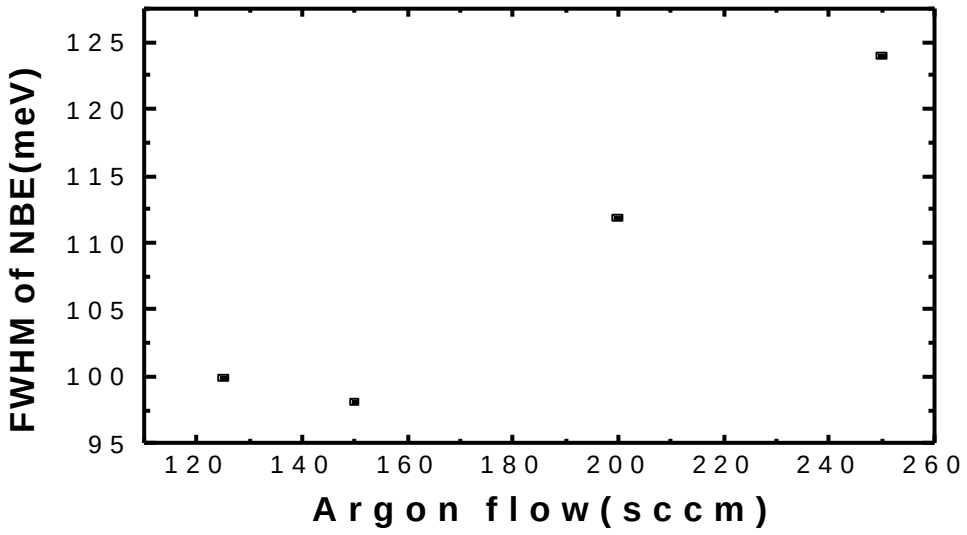

Fig.4-4: Argon flow dependent ZnO PL peak FWHM.

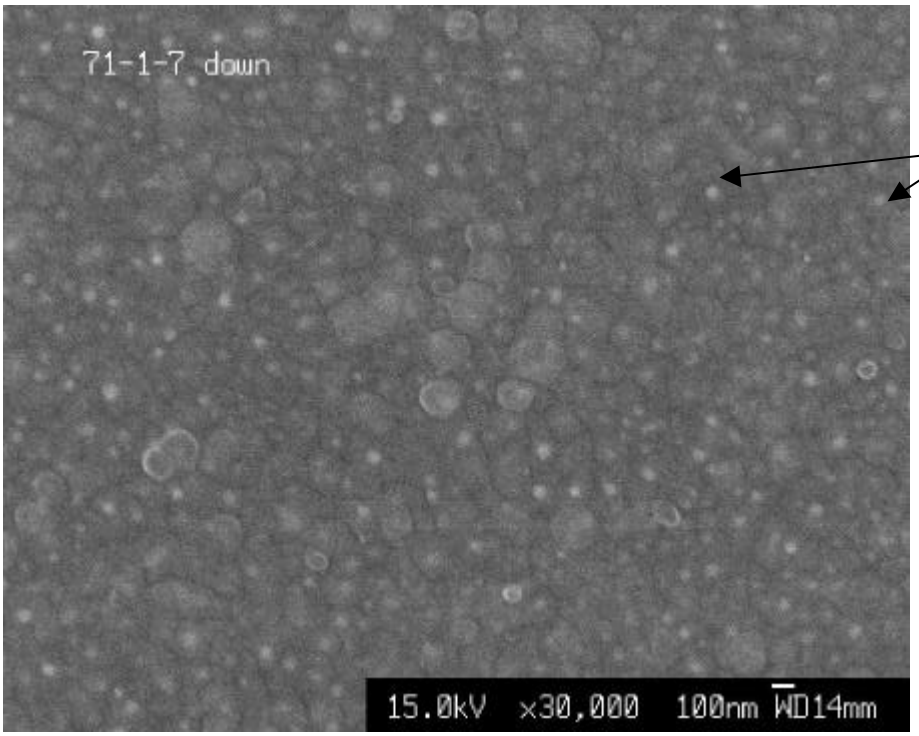

Fig.4-5: the SEM images of Au-Zn droplet-like on PS at high temperature.

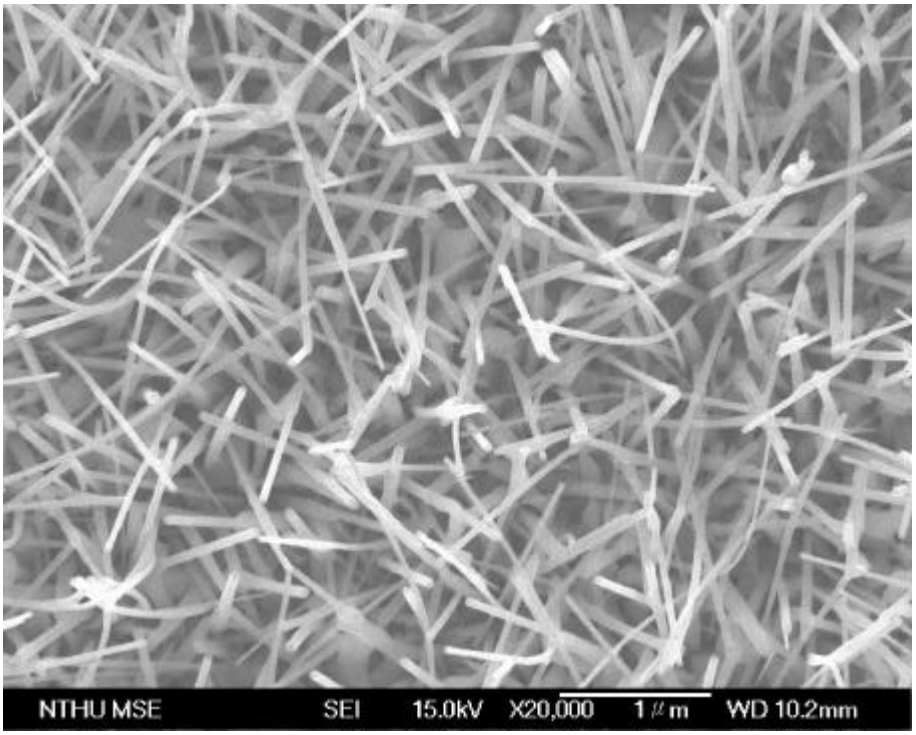

Fig.4-6: the SEM image of ZnO nanowires grown on the Au ~30Å coating PS.

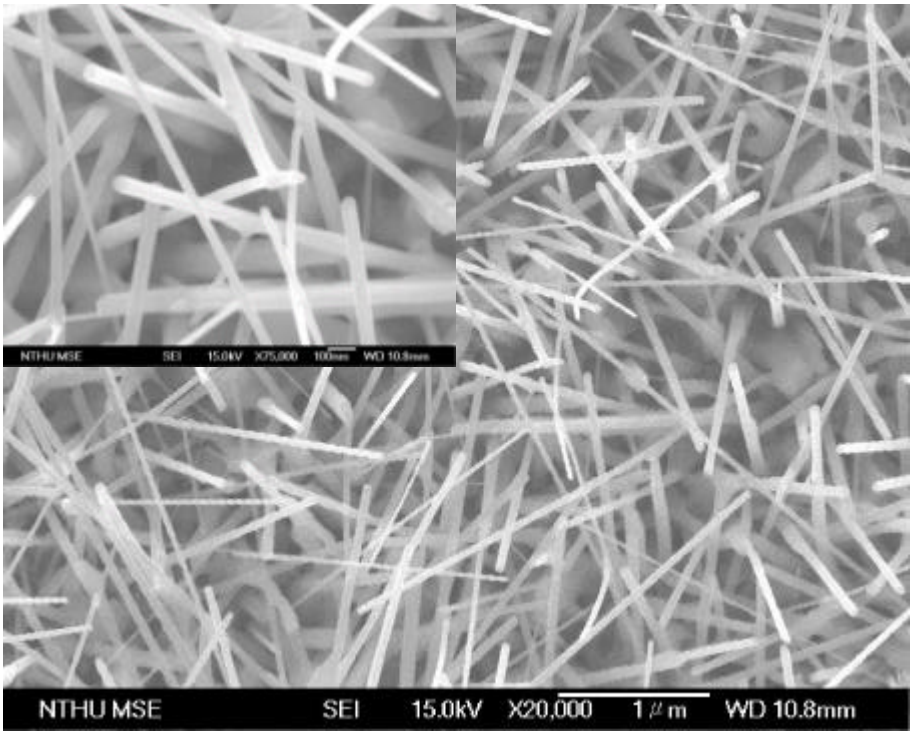

Fig.4-7: the SEM image of ZnO nanowires grown on the Au ~120Å coating PS.

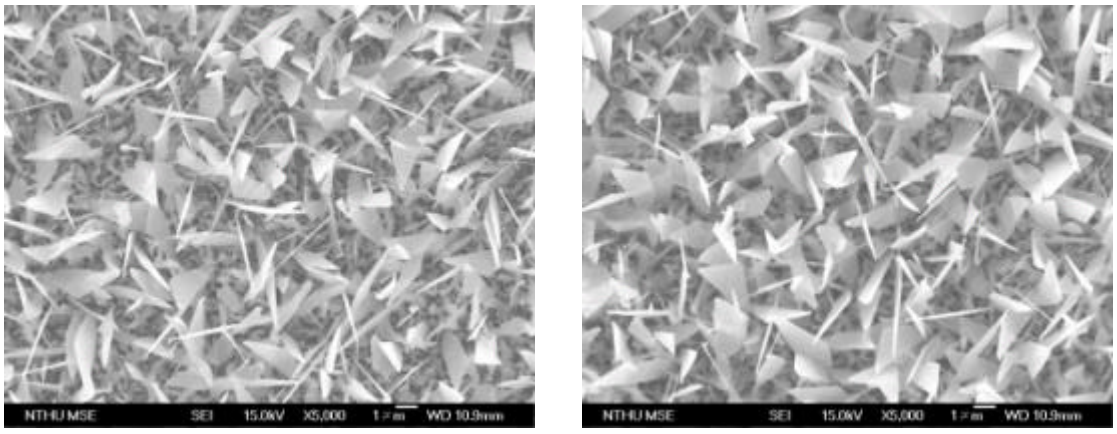

Fig.4-8: the SEM image of ZnO nanowires grown on the Au ~210Å coating PS.

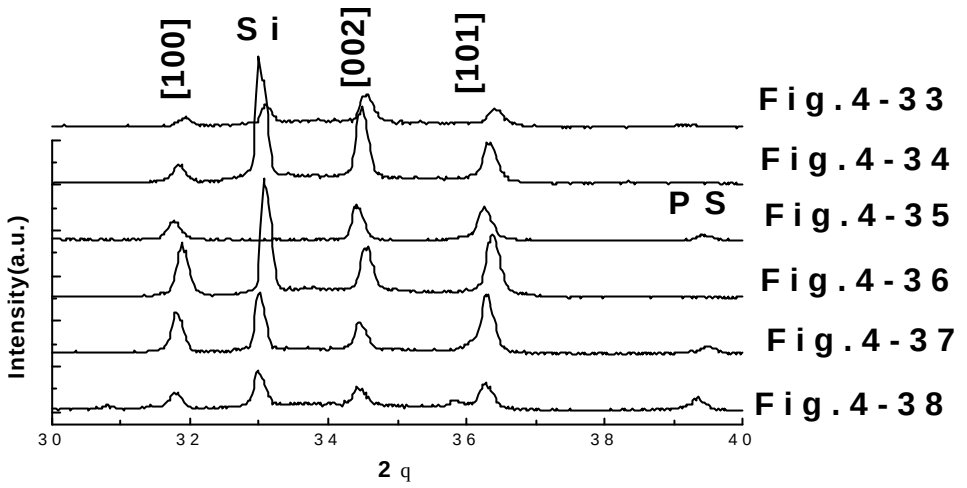

Fig.4-9(a): the XRD patterns of the ZnO nanowires.

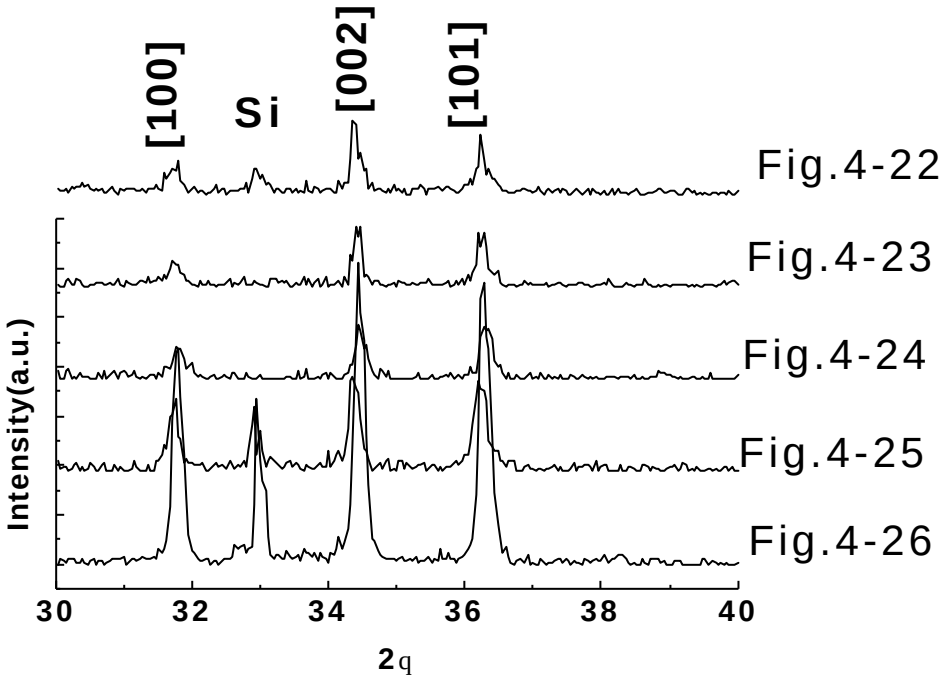

Fig.4-9(b): the XRD patterns of the ZnO nanowires grown on different PS substrates

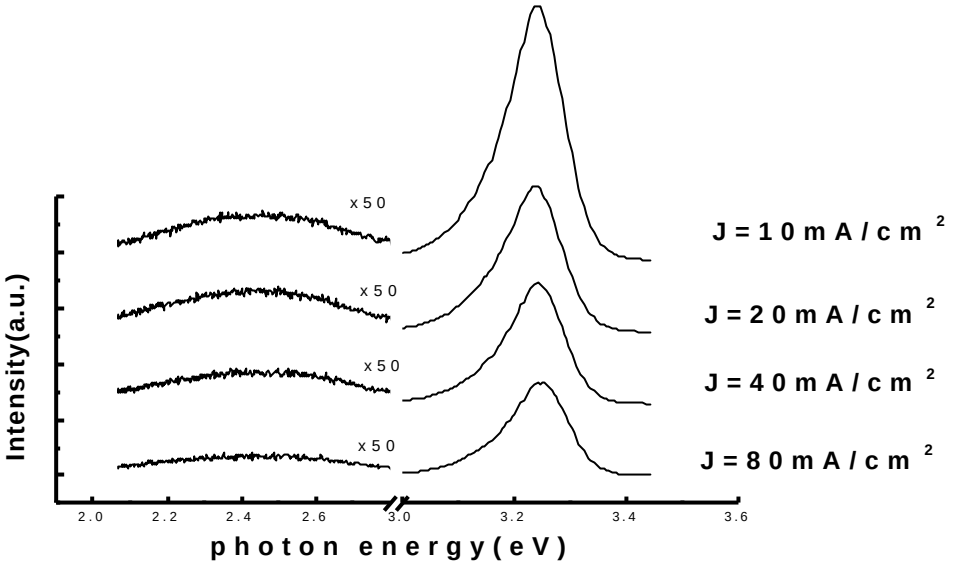

Fig.4-10: the PL spectra of a series of different current density PS substrates

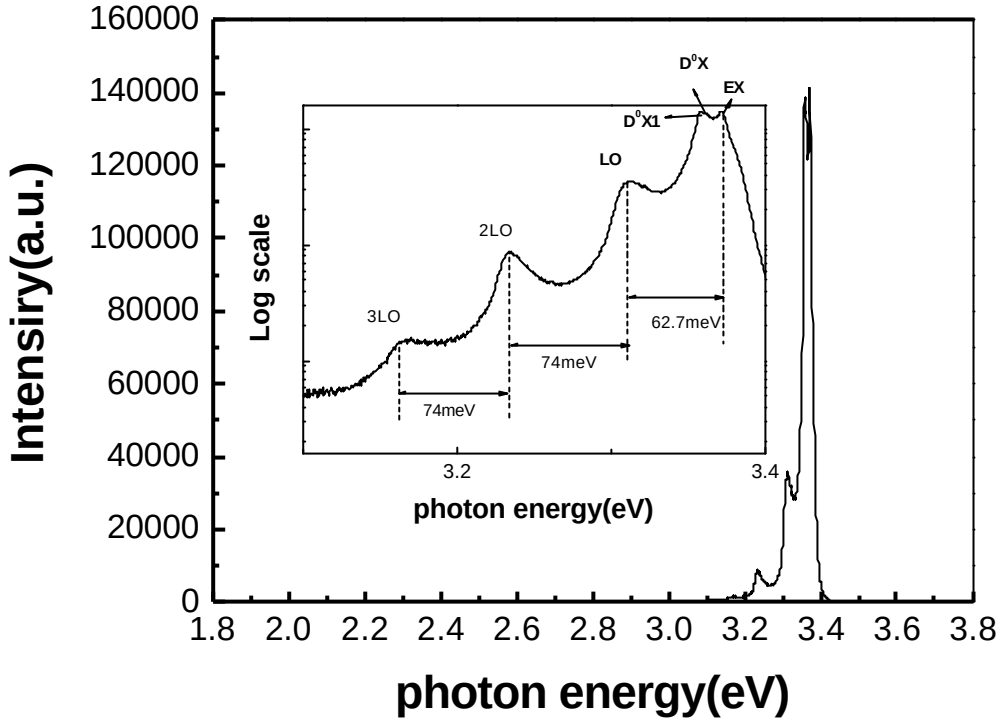

Fig.4-11: PL spectra at 7 K showing NBE, grew at a fixed 150sccm argon flow and 10 Torr in the growth time 4 hr. Insert shows detailed view of NBE.

Table

Spectrum mechanism	EX	D^0X	D^0X1	LO	2LO	3LO
position(eV)	3.3725	3.362	3.358	3.311	3.2335	3.1632

Table: show the emission mechanism and positions of spectrum.

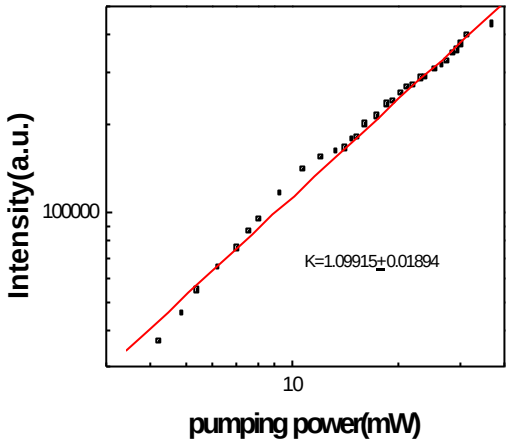

Fig.4-12 : The intensity of the free exciton PL vs. the power of exciting laser radiation

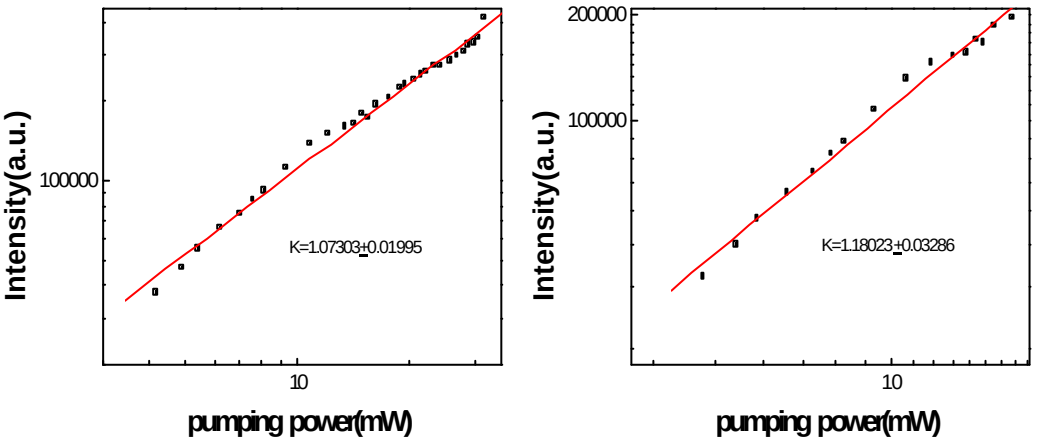

Fig.4-13~14: The intensity of the bound exciton PL vs. the power of exciting laser radiation.(left graph: D^0X; right graph: D^0X1)

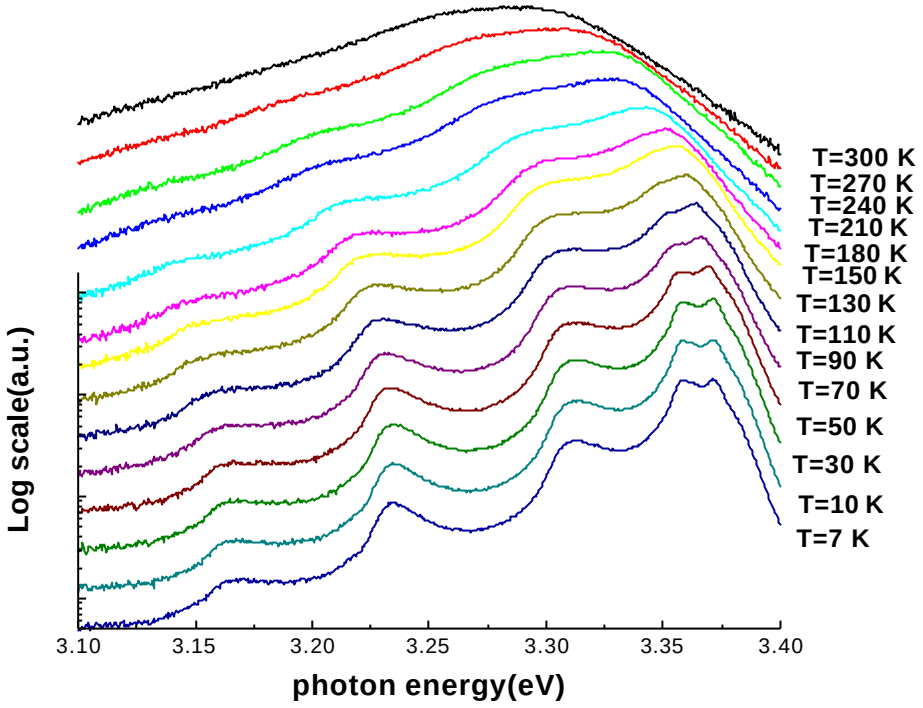

Fig.4-15: Emission spectra of the ZnO nanowires at the temperature range 7~300 K.

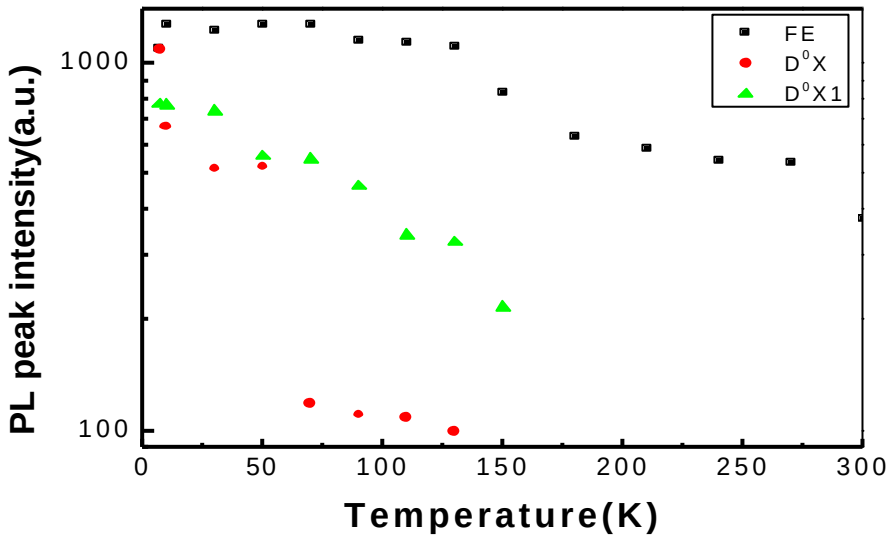

Fig.4-16: Temperature dependent PL intensities of nanowires.

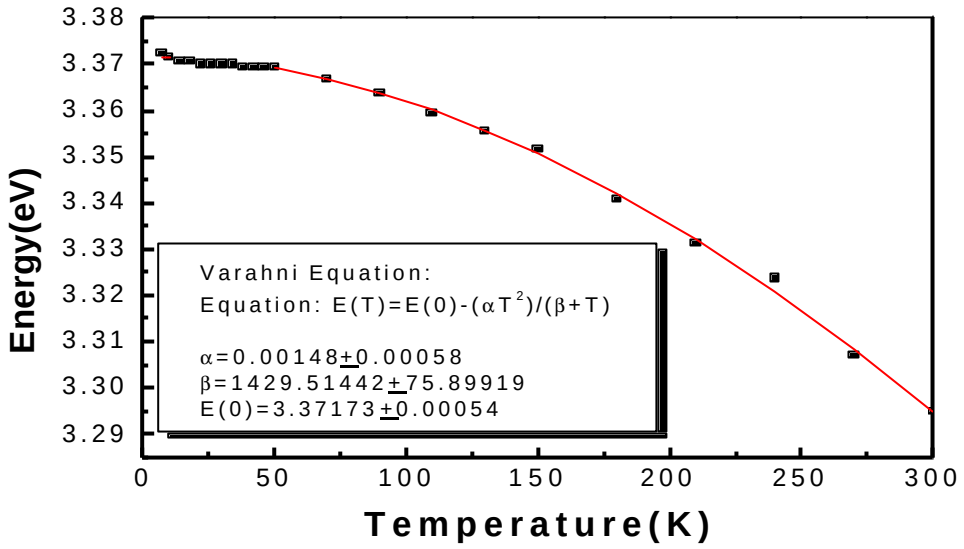

Fig.4-17: Evolution of the energy position of the free exciton as function of temperature(¦)data, (-)the fitting using the above Eqs.

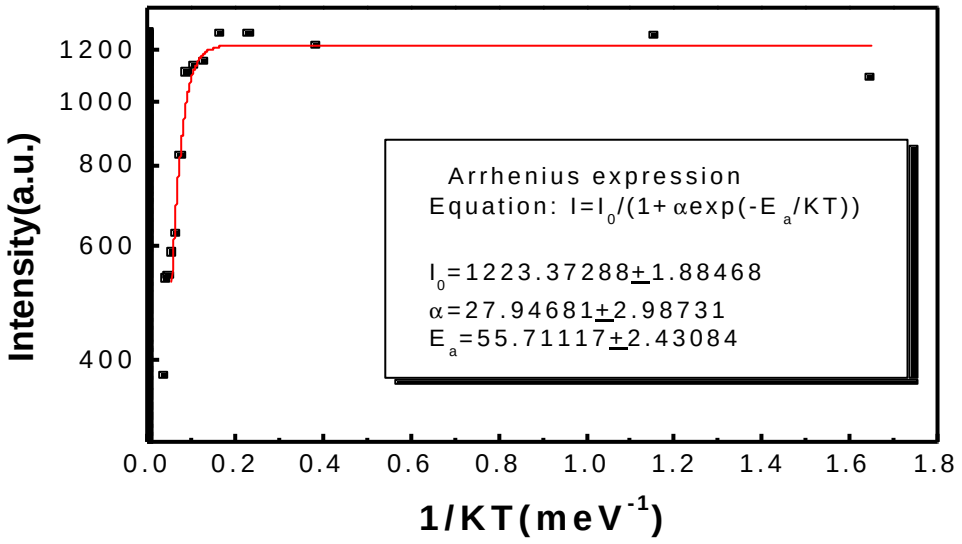

Fig.4-18: Temperature dependences of the free exciton of ZnO nanowires with theoretical fitting curve.

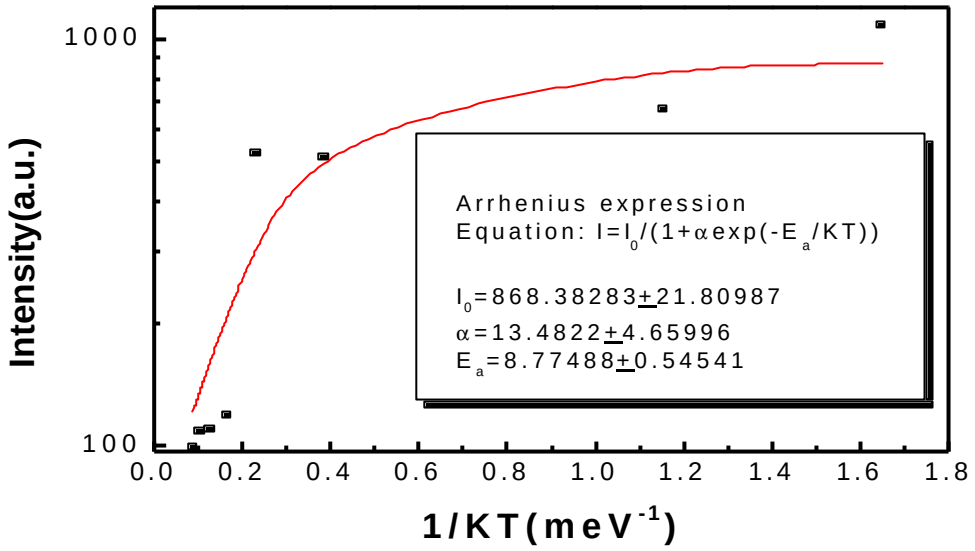

Fig.4-19: Temperature dependences of the bound exciton(D^0X) of ZnO nanowires with theoretical fitting curve.

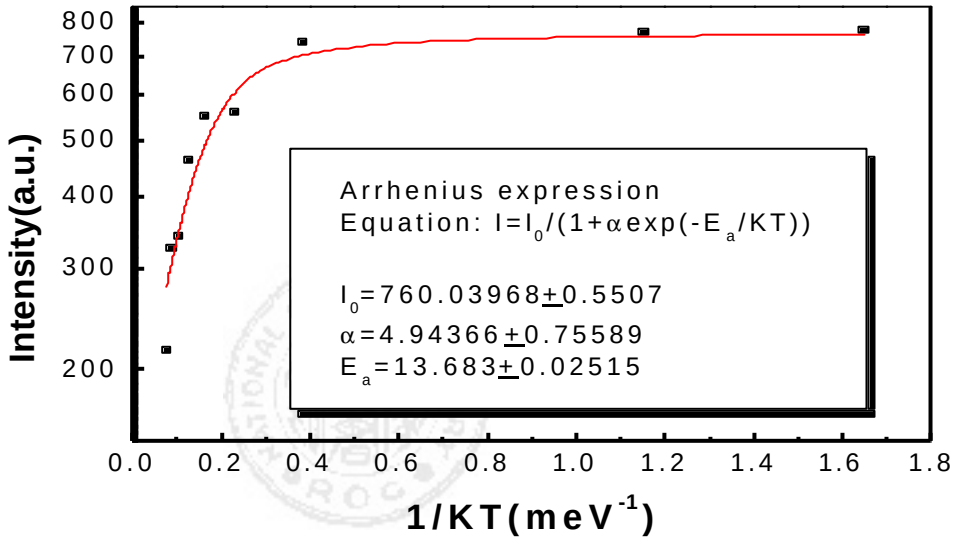

Fig.4-20: Temperature dependences of the bound exciton(D^0X1) of ZnO nanowires with theoretical fitting curve.

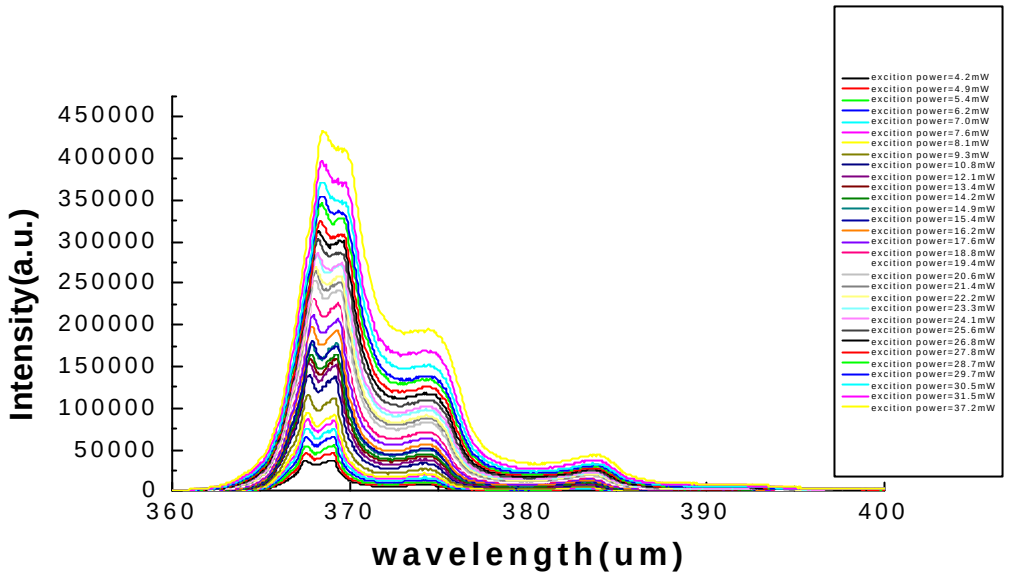

Fig.4-21: The PL spectra vs. the power of exciting laser radiation at 7 K.

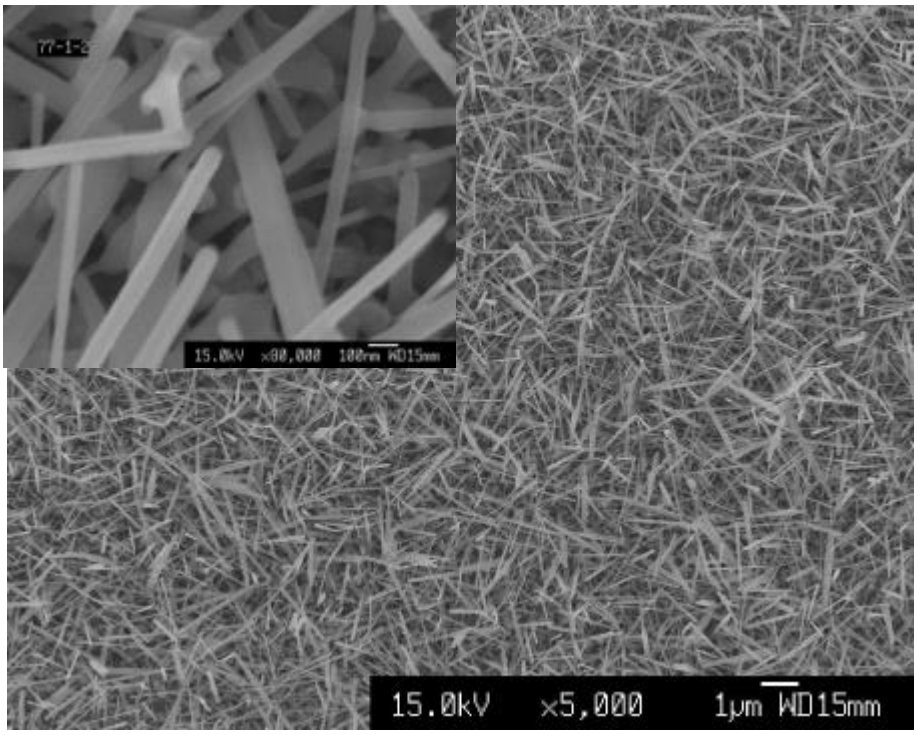

Fig.4-22: ZnO nanowires grown on the porous silicon substrate: 10mA/cm^2

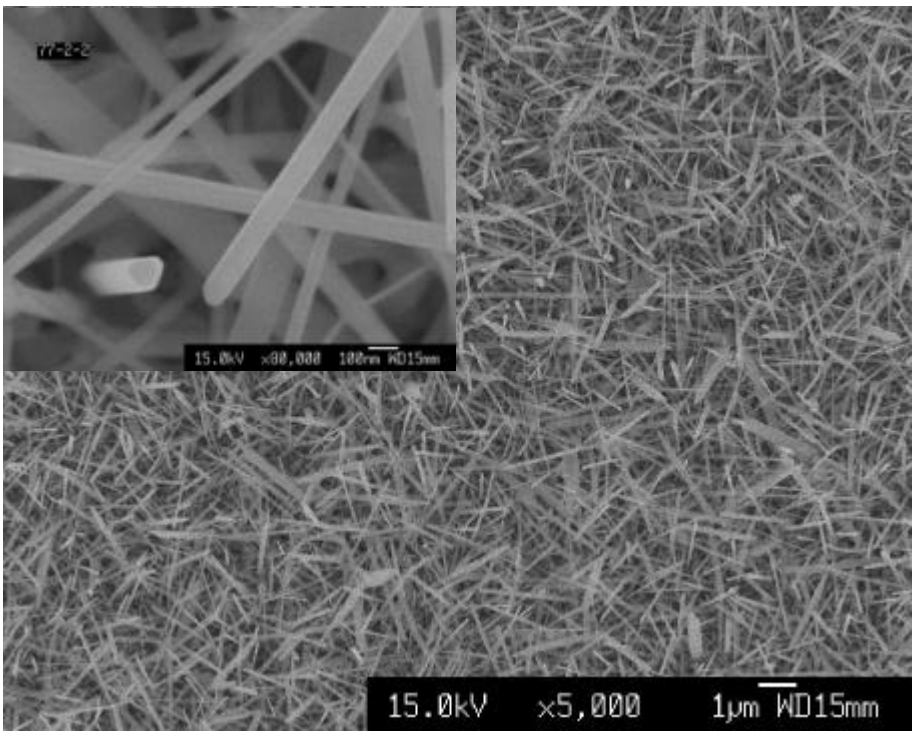

Fig.4-23: ZnO nanowires grown on the porous silicon substrate: 20mA/cm^2

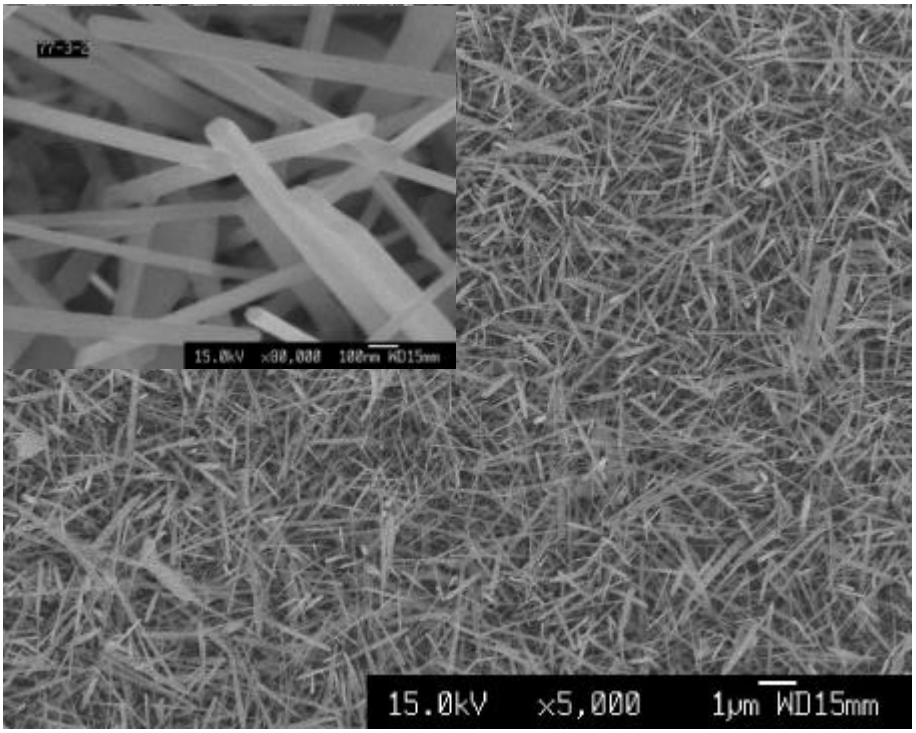

Fig.4-24: ZnO nanowires grown on the porous silicon substrate: 40mA/cm^2

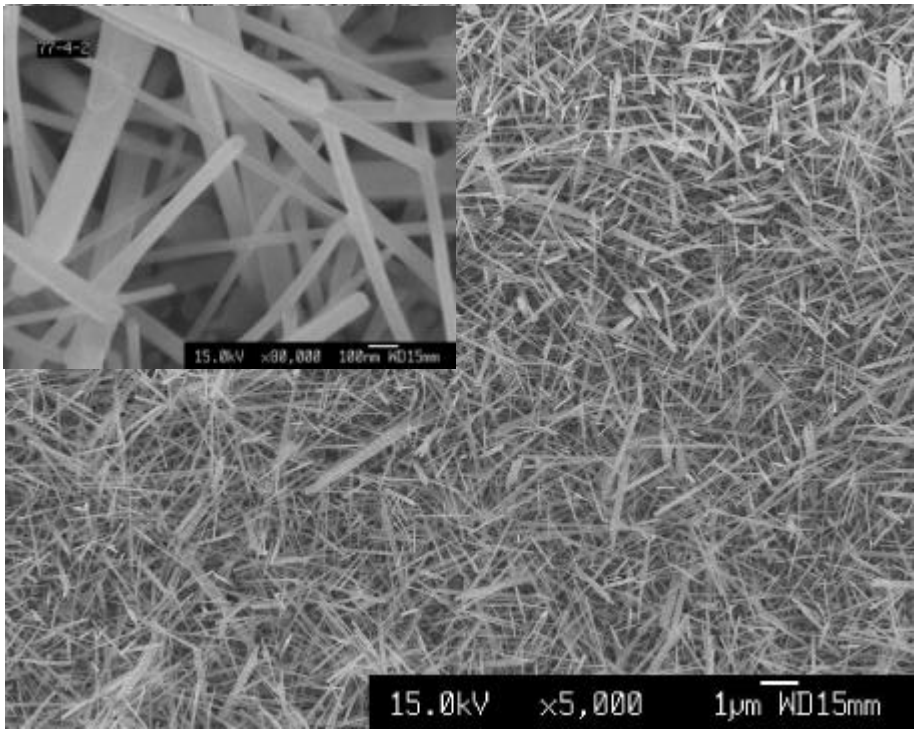

Fig.4-25: ZnO nanowires grown on the porous silicon substrate: 80mA/cm^2

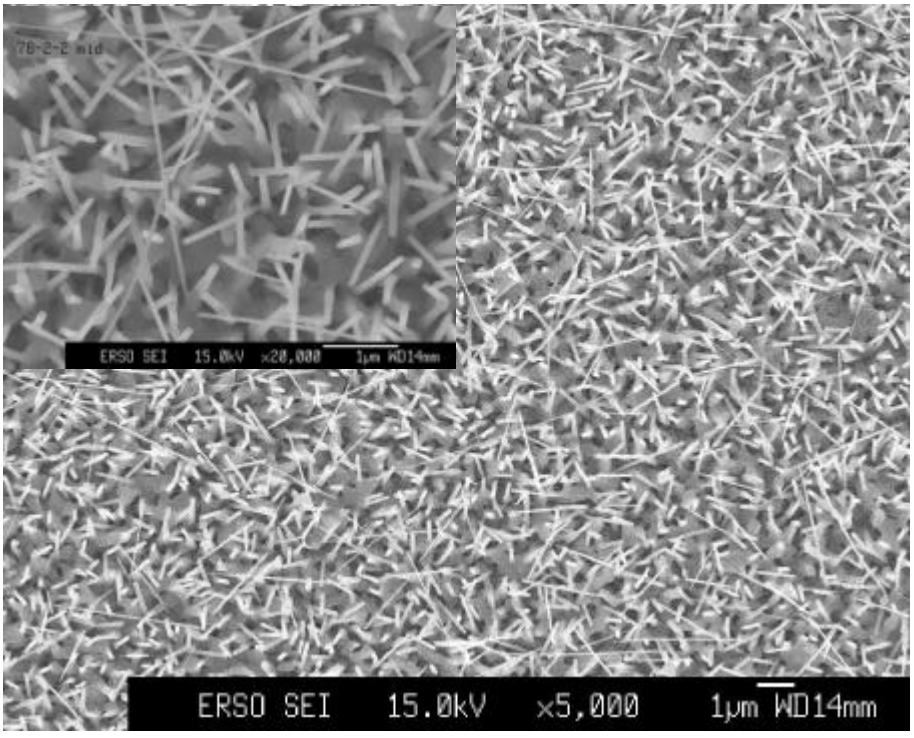

Fig.4-26: the SEM pattern for ZnO nanowires grown on silicon

Fig.4-27

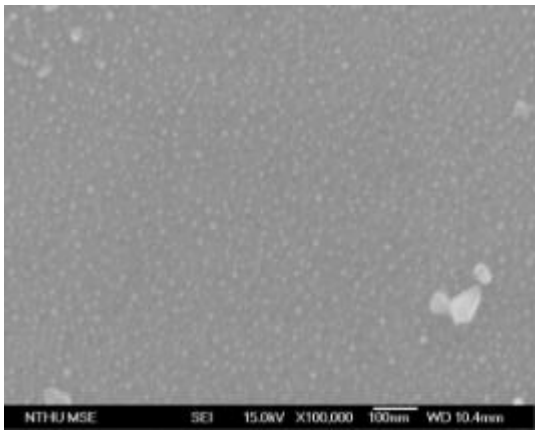

Fig.4-28

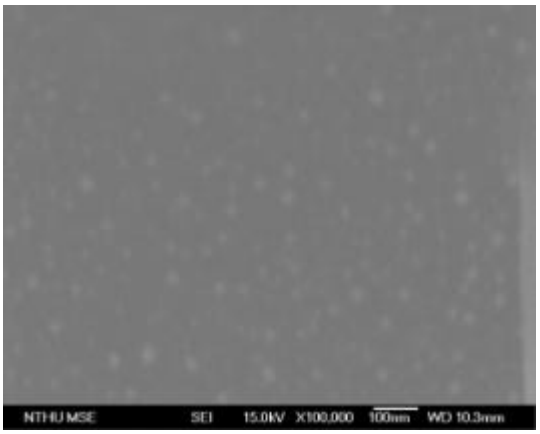

Fig.4-29

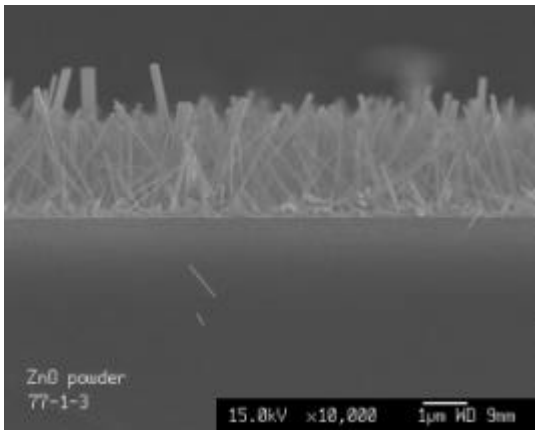

Fig.4-30

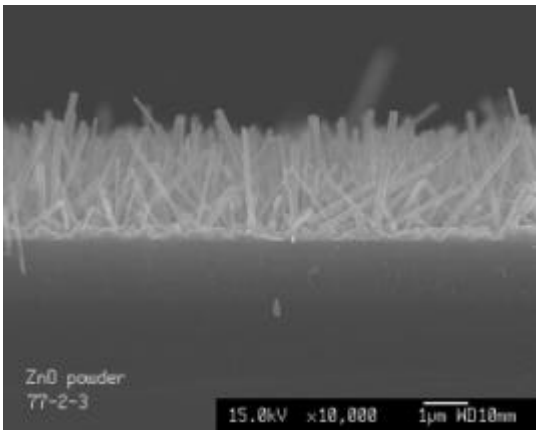

Fig.4-31

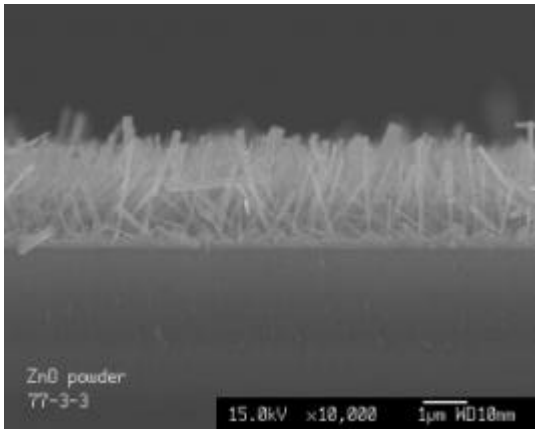

Fig.4-32

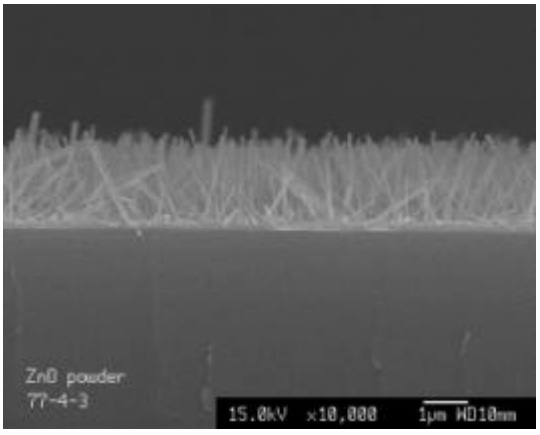

Fig.4-27~28: the SEM pattern for Au clusters on porous and pure silicon after annealing (left graph: porous silicon; right graph: silicon).

Fig.4-29~32: the cross-section SEM pattern for nanowire grown on different porous silicon substrates:(a)10mA/cm^2(b)20mA/cm^2(c)40mA/cm^2(d)80mA/cm^2

Fig.4-33

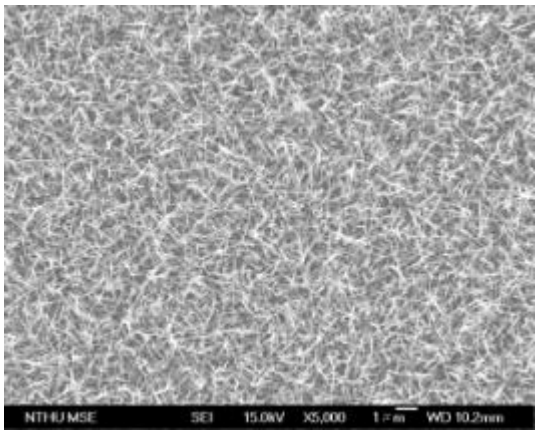

Fig.4-34

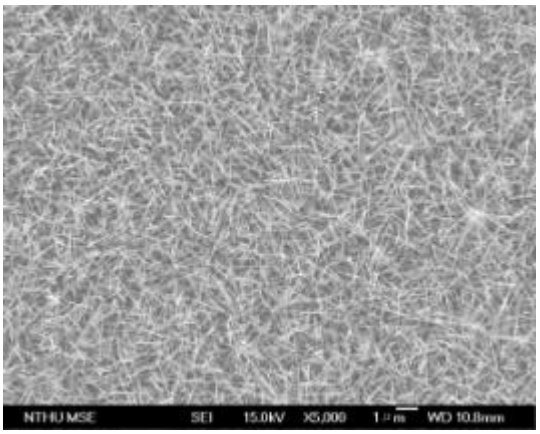

Fig.4-35

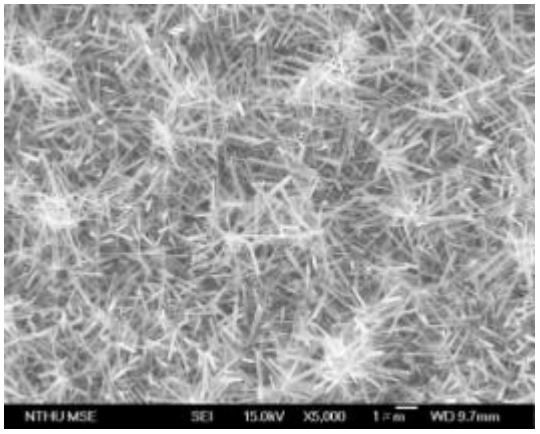

Fig.4-36

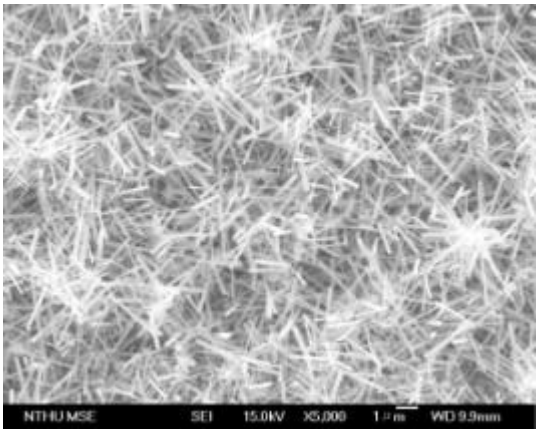

Fig.4-37

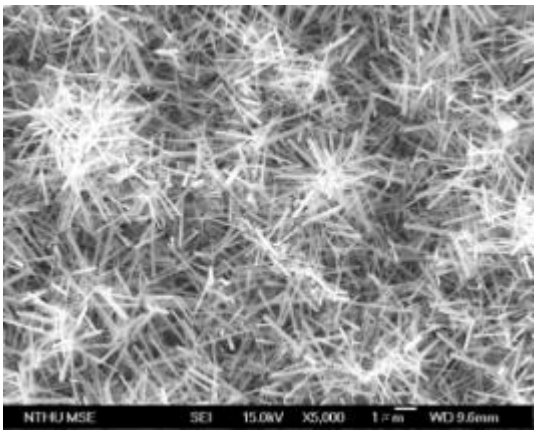

Fig.4-38

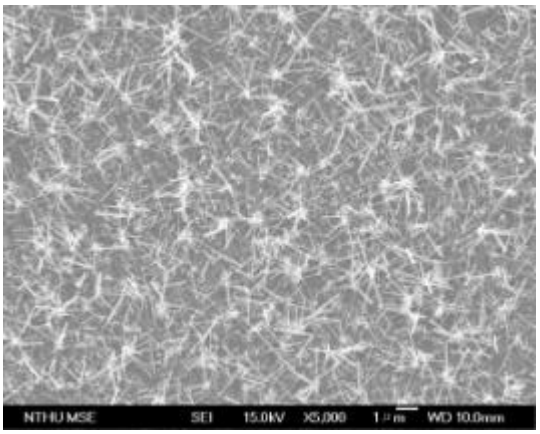

Fig.4-33~38: the SEM images of nanowires

Fig.4-39

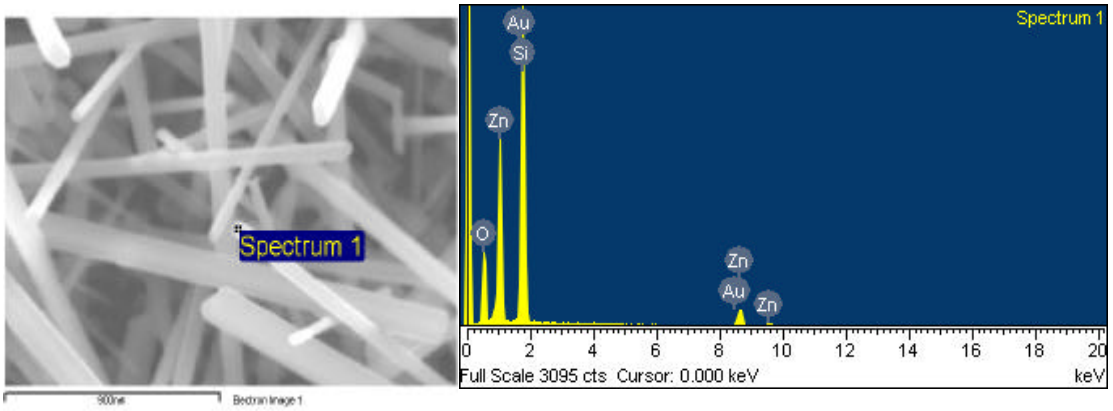

Element	Weight%	Atomic%
O K	21.01	39.36
Si K	40.61	43.32
Zn L	37.47	17.18
Au M	0.91	0.14
Totals	100.00	

Fig.4-40

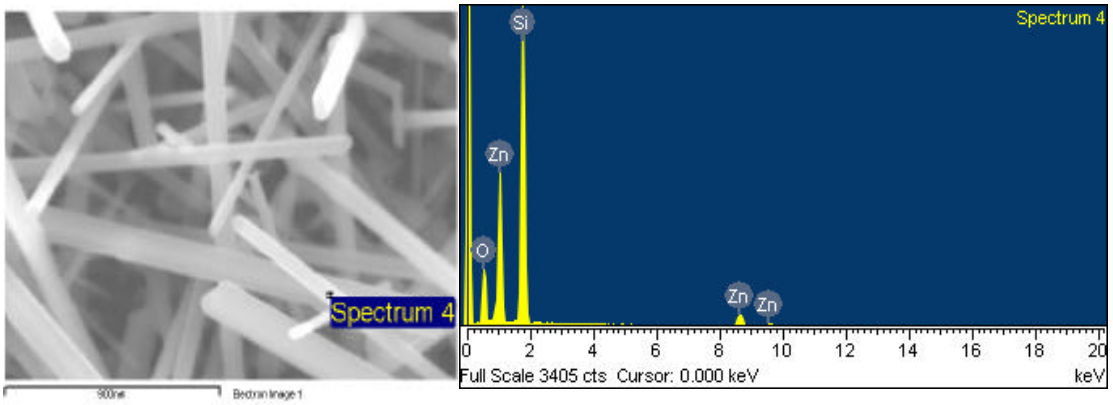

Element	Weight%	Atomic%
O K	19.81	36.39
Si K	46.16	48.31
Zn L	34.04	15.30
Totals	100.00	

Fig.4-39~40: the EDX pattern for ZnO nanowires

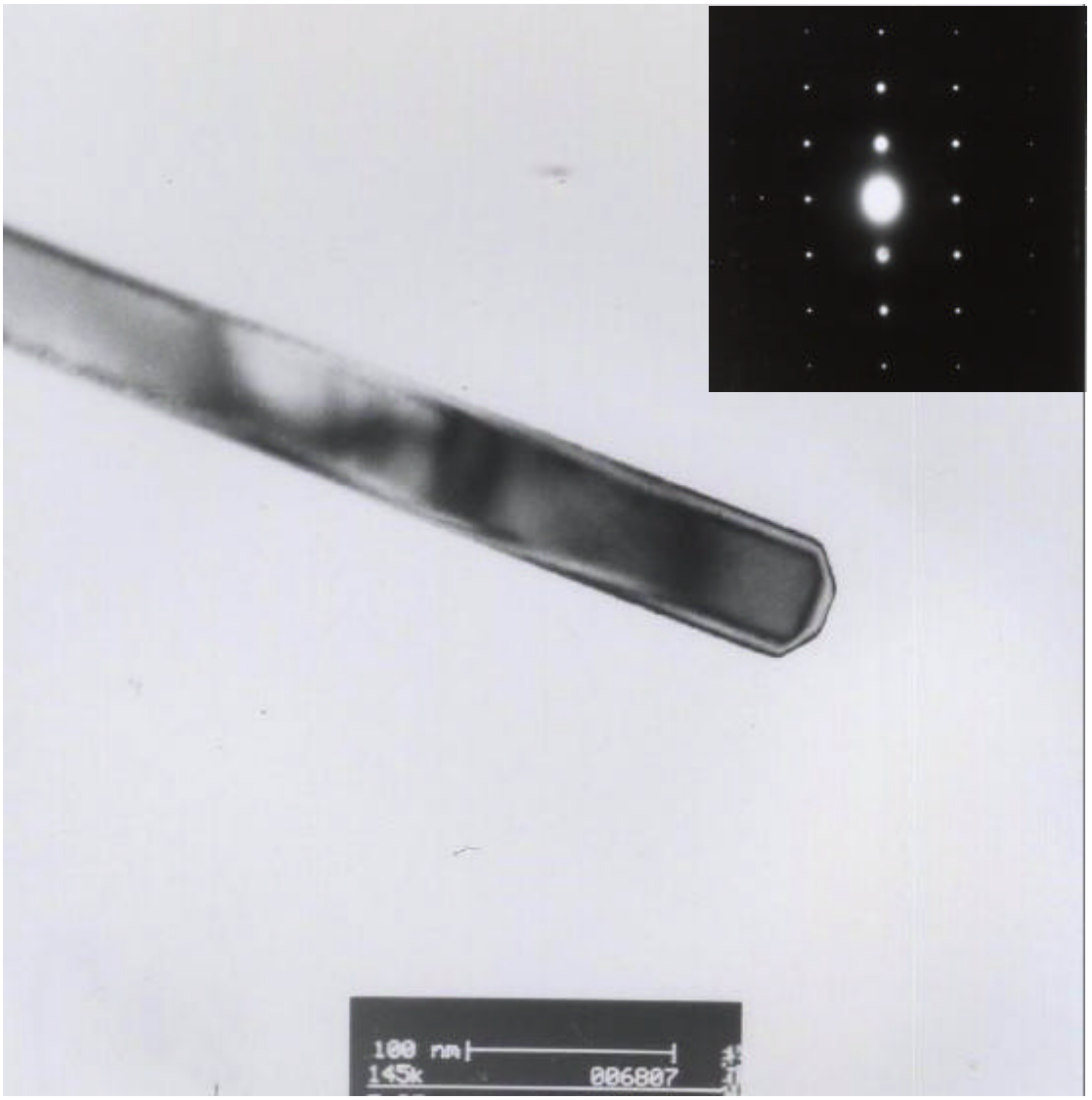

Fig.4-41: TEM image of a nanowire. The insert of Fig.4-41 is the SAED pattern

Table4-1(a)

$$T_{c(hkl)} = \frac{I_{(hkl)} / I_{0(hkl)}}{\frac{1}{N}\Sigma_N (\frac{I_{(hkl)}}{I_{0(hkl)}})}$$

sample	Fig.4-33	Fig.4-34	Fig.4-35	Fig.4-36	Fig.4-37	Fig.4-38
$T_{c(0\ 0\ 2)}$	2.014	2.0709	1.5976	1.2567	1.069	1.461

Table4-2(b)

Sample	Fig.4-26	Fig.4-22	Fig.4-23	Fig.4-24	Fig.4-25
Sample(mA/cm2)	0	10	20	40	80
Tc(002)	1.22	1.48	1.452	1.3027	1.18

Table4-2

$I \sim L^k$

Spectrum mechanism	FE	D^0X	D^0X
k	1.09915	1.07303	1.18023

Table4-3

	D^0X	D^0X1
Difference due to theoretical fitting (meV)	8.77448	13.683
Difference between peaks on the spectrum (meV)	8.6611	13.14812

Table4-1(a): the texture coefficient of ZnO nanowires

Table4-1(a): the texture coefficient of ZnO nanowires grown on different PS substrates

Table4-2: show the spectrum mechanism and k.

Table4-3: the activation energy of bound excitons and difference between EX and D^0X, D^0X1